First Principles Study of Structure, Defects and Proton Insertion in MnO_2

by

Dinesh Balachandran

B.Tech, Indian Institute of Technology, Bombay (1999)

Submitted to the Department of Materials Science and Engineering
in partial fulfillment of the requirements for the degree of

Master of Science in Materials Science and Engineering

at the

MASSACHUSETTS INSTITUTE OF TECHNOLOGY

August 2001
[September 2001]

© Massachusetts Institute of Technology, 2001. All rights reserved.

Author .....
Department of ~~Materials Science~~ and Engineering
August 24, 2001

Certified by 8/24/01
Gerbrand Ceder
Union Minière Professor of Materials Science and Engineering
Thesis Supervisor

Accepted by ....
Harry L. Tuller
Professor of Ceramics and Electronic Materials
Chair, Departmental Committee on Graduate Students

MASSACHUSETTS INSTITUTE OF TECHNOLOGY
JUN 17 2002
LIBRARIES

ARCHIVES

First Principles Study of Structure, Defects and Proton Insertion in MnO_2

by

Dinesh Balachandran

Submitted to the Department of Materials Science and Engineering
on August 20, 2001 in partial fulfillment of the
requirements for the degree of
Master of Science in Materials Science and Engineering

Abstract

We present an extensive First Principles study of structure, defects and proton insertion in MnO_2. It is shown that the paramagnetic extrapolations of spin-polarized results are essential to correctly reproduce pyrolusite as the ground state of MnO_2. While many other structures are found to be near degenerate in energy with pyrolusite, no thermal disorder exists in the system up to several thousand degrees as the strong correlation of the Mn-vacancy order along the lines of face sharing octahedra removes any low-energy excitations from the system. Mn-vacancies compensated by protons, ubiquitously present in commercial MnO_2 have a dramatic effect on phase stability and induce the formation of ramsdellite MnO_2 and twinning defects. We believe these proton compensated Mn vacancies to be the source of the structural complexity of synthetic MnO_2 produced either electrochemically or chemically.

It is shown that protons are always covalently bonded to an oxygen atom in MnO_2. In ramsdellite, the proton prefers the pyramidal oxygen to the planar coordinated oxygen atom. In both pyrolusite and manganite, the protons may appear to be at an octahedral center in experiments as the activation barrier for hopping between the two stable sites on each side of the octahedral position is only about 25 meV.

Introduction of de Wolff disorder and twinning defects is found to have a large adverse effect on the diffusivity of protons in γ-MnO_2. Protonation also increase barriers to proton migration due to Jahn-Teller distortion and H-H interactions. Results indicate that direct H-H interactions are not that significant compared to oxygen mediated indirect interactions, observed in manganite.

Experimental and calculated ramsdellite discharge curves deviate significantly at the early stages of the reduction process. We believe that a significant source of this discrepancy is the presence of proton compensated Mn vacancies in real MnO_2, which create local sites with higher discharge potential. Calculations also suggest that the ordered phase, observed in experiments at mid-reduction (groutellite, $MnOOH_{0.5}$), may be due to lattice remaining coherent during intercalation.

Acknowledgements

I would foremost like to thank my advisor, Gerd Ceder, for giving me the opportunity to conduct research with him and providing me with valuable guidance. His creativity and passion for research were an invaluable inspiration throughout my graduate career.

I express special thanks to Dane Morgan for his enormous help in my research. Dane displayed boundless patience and made me a better researcher than I would have otherwise been had I not had the opportunity to work along with him.

I am grateful to the other members of my group: Axel van de Walle for generously letting me use his codes; Anton Van Der Ven for helping me at various stages of my research; John Reed for his friendliness, Eric Wu for his excellent maintenance of the computers and for all his help; Chris Marianetti for being the "group entertainer", Stefano Curtarolo for his indomitable spirit and for his hospitable nature, Byungchan Han for being the nice guy that he is; Ashley Predith for helping keep spirits high and Elena Arroyo for her valuable comments.

Outside of lab, I would like to thank my friends for helping me understand that while research and science are both meaningful, we all have other aspects of our life as well. Deepak Khetpal helped me in innumerable ways and his friendship is something that I will always treasure. Chaitanya Ullal and I go a long way back and I am ever grateful for his constant help, admonition as well as encouragement. Sundararaman Subramanian and Rahul Raman were great friends and I will always cherish the wonderful moments that I shared with them.

I would like to acknowledge and thank my parents and family for their constant love and encouragement and also for their regular calls and letters. I hope they forgive me for being so lax in corresponding with them.

Last but certainly not the least, I would like to thank Prakriti Tayalia for being the most wonderful and supportive friend that I could ever imagine. She knew how to light a fire under me when I was lacking enthusiasm and her visits were highlights during my time here.

Contents

Chapter 1

Introduction

A battery is a device that converts the chemical energy contained in its active materials directly into electric energy by means of an electrochemical oxidation-reduction (redox) reaction. This type of reaction involves the transfer of electrons from one material to another through the electric circuit.

The battery cell consists of three major components [1]:

- The anode or the negative electrode- It is the electrode which gives up electrons to the external circuit and is oxidized during the electrochemical reaction.
- The cathode or positive electrode- It is the electrode which accepts electrons from the external circuit and is reduced during the electrochemical reaction.
- The electrolyte- It is the medium for transfer of charge, as ions, inside the cell between the anode and the cathode.

The most advantageous combinations of anode and cathode materials are those that will be lightest, least expensive, and give a high cell voltage and capacity. In a practical system, the anode is selected with the following properties in mind: efficiency as a reducing agent, compatibility with electrolyte, high coulombic output (Ah/g) and good conductivity. Mainly metals are used as the anode material. The cathode must be an efficient oxidizing agent, be stable in contact with electrolyte, and have a useful working voltage. Most of the cathode materials are metallic oxides, though other cathode materials are used for advanced battery systems giving high voltages and capacity. The electrolyte must have good ionic conductivity but must not be electrically conductive, as this would

cause internal-short-circuiting and self-discharge. Most electrolytes are aqueous solutions, though solid electrolytes are also used in some batteries [1].

1.1 Alkaline-Manganese Dioxide Batteries

Since it's introduction in the early 1960s, the alkaline-manganese dioxide battery has advanced to a dominant position in the primary battery market [1]. The alkaline battery is a convenient, relatively inexpensive source of packaged power for portable electronic devices, photographic equipment, toys and a host of other applications.

The active materials in the alkaline battery are manganese dioxide, an aqueous alkaline electrolyte, and powdered zinc metal. Manganese dioxide, which is used as the cathode, is the source of the oxidizing component in the battery. The only type of manganese dioxide that is used in commercial alkaline cells is electrolytic manganese dioxide (EMD, a form of γ-MnO_2). Electrolytic MnO_2 is used instead of either chemical MnO_2 or natural ore because of its higher manganese content, its increased reactivity, and its greater purity. Zinc is used as the anode material because of its good electrochemical behavior, compatibility with electrolytes, reasonably good shelf life and low cost.

The chemistry of the alkaline battery is based on the anodic oxidation of Zn to $Zn(OH)_2$, and proton insertion of MnO_2 to MnOOH on the cathodic side, though formation of Mn_3O_4 is also possible under slow discharge. The total cell reaction on continuous discharge to the depth of one electron per mole of MnO_2 can be formally written as:

$$2MnO_2 + Zn + H_2O = 2MnOOH + Zn(OH)_2 \qquad (1.1)$$

The focus of this research has been on the cathodic material. For the first electron transfer (per Mn), the cathodic half-cell reaction can be written as:

$$MnO_2 + H_2O + e = MnOOH + OH^- \quad (1.2)$$

At a lower voltage, MnOOH can then be discharged further, as in the following reaction:

$$3MnOOH + e = Mn_3O_4 + OH^- + H_2O \quad (1.3)$$

1.2 Motivation and Overview

The focus of this work has been to investigate the thermodynamics, kinetics and crystallographic aspects of proton insertion in γ-MnO_2 from first principles. While γ-MnO_2 has been the subject of experimental investigation for many years, remarkably little is known about its structure and other relevant properties. γ-MnO_2 has been described as built up from pyrolusite elements interspersed in a ramsdellite matrix, whereas other authors have proposed that γ-MnO_2 includes a partially ordered version of ε-MnO_2 in addition to ramsdellite and pyrolusite (the various structures for MnO_2 will be discussed subsequently in Chapter 3). These structural peculiarities, whose details are largely unknown, as well as the poor quality of X-ray diffraction patterns obtained from most samples, explains why γ-MnO_2, in general, is a poorly characterized material. In the present work, we demonstrate the use of First Principles calculations to investigate the various polymorphs of γ-MnO_2 and try to understand the reasons for its structural complexity. The calculations show that structural complexity in γ-MnO_2 is not simply due to thermal disorder. The calculations also suggest that Mn defects could be a reason for the structural complexity.

Concerning electrochemical properties, discharge of the alkaline battery occurs through proton and electron insertion into the host γ-MnO_2 structure. Although γ-MnO_2 is, strictly speaking, not a homogeneous phase, since the presence of extended structural defects implies the existence of several non-equivalent Mn sites in the lattice, it is still

frequently accepted that this insertion process occurs homogeneously and that a single phase is obtained as final product after insertion of one electron per Mn atom [2]. This statement can be largely attributed to the lack of accurate structural characterization of the pristine and reduced materials. In the present work, we have used computational methods to investigate the electrochemical properties of γ-MnO_2.

The thesis is organized into 5 chapters. In Chapter 2, we describe the methodology used to perform the computations. These include First Principles calculations, cluster expansion formalism and Monte Carlo simulations.

Chapter 3 reviews the structural stability of γ-MnO_2. The dominant interactions in the system are identified and Monte-Carlo simulations are performed in order to identify the ground state, nature of excitations and the transition temperature for Mn-vacancy disorder in γ-MnO_2. The effect of proton compensated Mn vacancies (Ruetschi defects) on the structural stability of γ-MnO_2 has also been discussed.

Chapter 4 deals with proton insertion dynamics in MnO_2. Proton locations and activation energy barrier for proton diffusion is determined for various MnO_2 and MnOOH polymorphs. In addition, the intercalation curve for ramsdellite is calculated and compared with experimental intercalation curves.

In Chapter 5, we summarize our results and offer suggestions for future research.

Chapter 2

Methodology

First-principles modeling refers to the use of quantum mechanics to determine the structure and properties of materials. In this chapter, we describe the use of first-principles methods to obtain information on the structural stability, proton diffusion characteristics, and voltage properties of γ-MnO_2 for primary alkaline batteries.

All of the work done in this study begins with first-principles calculations at 0 K to determine the total energy of various MnO_2 and $MnOOH_x$ polymorphs. In order to determine the thermal disorder and calculate detailed proton insertion curves, a free energy model is constructed to calculate behavior at non-zero temperatures. A cluster-expansion based on the 0 K total energies is built to parameterize the energy as a function of manganese or proton arrangement. The interactions obtained from the cluster expansion are then used in conjunction with Monte Carlo simulations, a standard statistical mechanics method, to determine thermal excitations and calculate voltage curves. In addition, elastic band calculations and molecular dynamics simulations are used to determine the proton diffusion path in various $MnOOH_x$ polymorphs.

2.1 First-Principles energy calculations

The equations that govern interactions between the electrons and nuclei of the solid have been well known for decades, but finding their exact solution for a complex solid is beyond the limits of current computing power. However, using a series of

approximations, the electronic structure and thus the total energy of most materials can be calculated quite accurately.

A wide variety of first-principles methods is used to determine the behavior of materials. Materials have different types of bonding interactions and therefore some approximations are better suited than others for a particular system of interest [3]. The modern quantum-mechanical techniques used here to compute total energies, are based on the density functional theory [4]. In principle, this framework allows us to exactly map the problem of solving the Schrödinger equation for many interacting electrons onto that of a single electron moving in a non-local potential. This potential is not known exactly and several approximations can be used to represent it. One of the most commonly used expressions is a local representation of the effective potential called the local-density approximation (LDA) [5]. However, the local-density approximation fails under certain conditions [6] and hence, the general gradient approximation (GGA) was developed [6] in an attempt to address the source of error in LDA. In this work, we solve the Schrödinger equation within the GGA by using the pseudopotential method. Although originally developed for metals and semiconductors, the accuracy of the pseudopotential method is now well established for use in oxides [7, 8, 9, 10, 11, 12]. It has been found previously that the total energies in these oxide systems can be well predicted with pseudopotential approximations. [7, 13, 14]

The Vienna Ab Initio Simulation Package (VASP) pseudopotential program [15, 16] used here solves the Kohn-Sham equations within the GGA using ultra-soft pseudopotentials [17, 18]. All crystallographic degrees of freedom are optimized such that the minimum ground state energy is obtained. The VASP program implements the Ceperley and Alder [19] exchange and functional correlation as parameterized by Perdew and Zunger [20] in the energy calculations. The method of Monkhorst and Pack [21] is

used to parameterize the k-space sampling. During relaxation calculations, the ionic positions and the lattice parameters of each structure are relaxed with the conjugate gradient method using forces and stresses. The energies of the optimized geometries are recalculated after each relaxation run, holding the atomic positions and the volume static. In these static runs, *k*-space integrations are performed using the linear tetrahedron method including corrections according to Blochl et al. [22]. For all calculations, the plane wave basis set cutoff energy was set to 405 eV.

2.2 Cluster Expansion formalism

2.2.1 Mn-vacancy lattice model

The γ-MnO_2 structure can be thought as consisting of a (possibly distorted) hexagonal close packed (hcp) oxygen framework with Mn and vacancies each occupying half of the hcp lattice's octahedral sites. The hcp octahedral sites can be shown to form a simple hexagonal lattice themselves and all the MnO_2 polymorphs relevant to γ-MnO_2 can be understood as different Mn-vacancy arrangements on this hexagonal lattice. There are many other MnO_2 polymorphs (e.g., those based on a face centered cubic lattice of oxygen) but these do not seem to appear in the γ-MnO_2 materials. Hence, the problem of understanding MnO_2 structures can be formally approached by investigating the ordered states of a binary alloy (Mn and vacancies are the constituents) on a simple hexagonal lattice.

To study defects and thermal disorder in MnO_2, the energy of many Mn-vacancy arrangements may need to be evaluated. Lattice models that parameterize the energy of Mn-vacancy arrangements can be quite convenient in this respect. Fortunately, the use of a lattice model to study the thermodynamics of MnO_2 can be well justified and extended

to arbitrary sets of interactions. In alloy theory [23] it has been shown that in systems with configurational (ionic disorder), a lattice model formalism arises naturally when coarse-graining the partition function of the system over faster degrees of freedom. To characterize a given Mn configuration for a structure, it is useful to introduce occupation variables σ_i for each lattice site i which is +1 if manganese occupies site i and −1 if site i is vacant. If we now let $\{\sigma\}$ represent a specific set of octahedral interstices that are occupied, and $\{\tau\}$ represents the state of all other degrees of freedom (e.g. positional, electronic, or magnetic), the partition function of the material can be written as:

$$Z = \sum_{\{\sigma\}} \sum_{\{\tau\{\sigma\}\}} \exp\left(\frac{-E(\{\sigma\},\{\tau\{\sigma\}\})}{kT}\right) \tag{2.1}$$

The first summation contains all the different possible distributions of Mn over the octahedral sites. The second summation is over the faster excitations that can exist in a given configuration $\{\sigma\}$. This ensemble of excitations is labeled as $\tau\{\sigma\}$. The effect of the fast excitations can be reduced to an *effective* configurational Hamiltonian $F(\{\sigma\})$ for the $\{\sigma\}$ degrees of freedom by formally replacing the inner sum: With

$$F(\{\sigma\}) = -kT \ln\left[\sum_{\{fast\{\sigma\}\}} \exp\left(\frac{-E(\{\sigma\},\{fast\{\sigma\}\})}{kT}\right)\right], \tag{2.2}$$

the partition function of the system becomes:

$$Z = \sum_{\{\sigma\}} \exp\left(\frac{-F(\{\sigma\})}{kT}\right) \tag{2.3}$$

Eqn. (2.3) is the partition function of a lattice model. Applying lattice model statistical mechanics to $F(\{\sigma\})$ will therefore give the thermodynamic properties of the true system. Eqn. (2.2) can be seen as one step toward systematically removing degrees of freedom from a system. $F(\{\sigma\})$ incorporates the effect of all vibrational, electronic, magnetic, etc. disorder and can be thought of as a *free energy* for these excitations in an

ensemble of fixed configuration $\{\sigma\}$. In the last step, (eqn. (2.3)) the effect of configurational disorder is then added. In many cases $F(\{\sigma\})$ will be approximated by the lowest energy term in the ensemble $\tau(\{\sigma\})$. This means the lowest energy state $E^{\circ}\{\sigma\}$ for a fixed configuration $\{\sigma\}$. Practically, this state is found by placing the Mn ions in configuration $\{\sigma\}$ on the ideal octahedral lattice and relaxing the system until the lowest energy is obtained. Such an approach amounts to neglecting all other entropy effects besides configurational entropy and is widely used in the first-principles calculation of phase diagrams. In this work, we will go beyond this approach and include the effect of magnetic excitations in the lattice model Hamiltonian (eqn. (2.2)). For the important low-energy Mn distributions in the octahedral site we will integrate over the disorder of the magnetic spins on the Mn^{4+} ions, since these materials are paramagnetic at room temperature and magnetism has been found to play an essential role in stabilizing the correct ground states in manganese oxides [24]. Vibrational entropy will not be included though it could be incorporated with methods proposed recently [25].

The description in terms of configurational variables $\{\sigma\}$ needs to be distinguished from one in terms of real positions of ions. The state $\{\sigma\}$ is only a label to describe which ion is associated with which lattice site (i.e. which octahedral interstice). It does not at all assume the ions to sit exactly at the sites of some "ideal" lattice. Rather, the label $\{\sigma\}$ represents the relaxed state of the ions in that configuration.

It is of course impossible to calculate $F\{\sigma\}$ for each possible configuration. For a system with N sites that can be occupied by 2 species there are 2^N possible configurations. Rather, the approach is to construct a rapidly converging expansion for $F\{\sigma\}$ in terms of a set of variables that describe the configurational state. Such a set of variables is given by the *cluster functions* [26]. For a collection of lattice sites (the cluster

α), the cluster function ϕ_α is defined as the product of all occupation variables in that cluster:

$$\phi_\alpha = \prod_{i \in \alpha} \sigma_i \tag{2.4}$$

If a cluster function for each possible cluster of sites on the lattice is included, this basis set of functions is complete [26] so that any property of configuration can be written in this basis up to arbitrary accuracy. Such an expansion is referred to as a *Cluster Expansion* (CE). This is somewhat of a misnomer as the clusters α are not clusters of atoms in a physical sense. They merely represent clusters of configurational variables in an infinite system. A more appropriate term would be to call it a *configurational* expansion. The thermal and spatial average of a cluster function (averaged over all the clusters that are equivalent by symmetry) is called a *correlation function.* For example, a state in which all Mn ions would have vacancies in the nearest neighbor position would always have this cluster function equal to $(+1)\cdot(-1) = -1$, and the correlation function would be -1. Correlation functions present a powerful way to numerically represent a structure and the correlations for common structures of MnO_2 are given in Table 1.

The energy can be expanded in cluster functions:

$$F(\{\sigma\}) = \sum_\alpha V_\alpha \phi_\alpha(\{\sigma\}) \tag{2.5}$$

The expansion coefficients V_α are referred to as effective cluster interactions (ECI). They have little to do with any *real* interaction or potential but are only coefficients in a parameterization of the energy $E^\circ\{\sigma\}$ in terms of the cluster functions. Practically, they are obtained by calculating the energy of a series of configurations $\{\sigma\}$ and then fitting a truncated form of eqn. (2.5) to the values of E° obtained. In this work, we use the cross-validation method to optimize the quality of the fit [25].

2.2.2 H-vacancy lattice model

For applications in a battery, the crucial property of γ-MnO_2 is the voltage curve as a function of proton concentration. The voltage is related to the chemical potential of proton within the cathode host (i.e. γ-MnO_2) according to:

$$\Phi = \Phi_0 - F^{-1}.\mu_H^{cathode} \tag{2.6}$$

where F is Faraday's constant, $\mu_H^{cathode}$ is the chemical potential of H in the cathode host and Φ_0 is a constant. With eqn. (2.6), the voltage can easily be determined from the chemical potential of proton in the cathode, and the relation between voltage measurements and thermodynamics is clear. Information about the intercalation profile can now be found from knowledge of the Gibbs free energy of proton in the cathode host.

In the previous section, we have shown how configurational energy can be described with a *cluster expansion*. Here, in order to study the intercalation process in ramsdellite, we again resort to the *cluster expansion* formalism. We identify the H-vacancy sublattice and determine the important H-vacancy interactions in ramsdellite. First principles calculations are then performed to determine energies of a set of different H arrangements, at various intercalation levels, in ramsdellite. The interactions are then fit to the first-principles energies to obtain values for the H-vacancy interactions in ramsdellite.

2.3 Monte Carlo simulations

Monte Carlo (MC) methods [27, 28, 29, 30, 31] are now a standard tool for numerical simulation. The basic idea of the MC approach is to use stochastic computer simulation to sample the states of a system with appropriate probabilities in order to

calculate the thermodynamic averages. For a lattice model, a Monte Carlo simulation samples different Mn-vacancy or H-vacancy configurations with relative frequencies given by the probability distribution function:

$$P_s = \frac{\exp\left(-H_s / k_B T\right)}{Z} \tag{2.7}$$

where Z is the partition function defined as:

$$Z = \sum_s \exp\left(-H_s / k_B T\right) \tag{2.8}$$

Here, H_s is the enthalpy of state s, T is the temperature and k_B is Boltzmann's constant. Sampling is achieved with a Markov chain of configurations where each configuration is derived from previous configuration according to a suitable transition probability.

The transition probability most often implemented is due to Metropolis [32]. The algorithm starts with an arbitrary configuration. New configurations are created by picking lattice sites either sequentially or at random and by changing the value of their occupation variable according to a pre-established rule in which a transition probability $w(i \rightarrow f)$ is compared to a random number between 0 and 1. i refers to the configuration before the transition and f corresponds to the configuration after the transition. For the Mn ions and vacancies on the octahedral sites of γ-MnO_2, a typical transition in the grand canonical ensemble would be a change in the value of an occupation variable of a particular Mn site from +1 (-1) to −1 (+1). A suitable transition probability is then:

$$w(i \rightarrow f) = 1 \qquad \Omega(\sigma_f) < \Omega(\sigma_i) \tag{2.9}$$

and

$$w(i \rightarrow f) = \exp\left(\frac{-\left(\Omega(\sigma_f) - \Omega(\sigma_i)\right)}{kT}\right) \qquad \Omega(\sigma_f) \geq \Omega(\sigma_i) \tag{2.10}$$

where Ω is the grand canonical energy defined as

$$\Omega(\sigma) = H(\sigma) - \mu N \tag{2.11}$$

$H(\sigma)$ is the enthalpy of configuration σ, μ is the chemical potential and N corresponds to the number of Mn ions in the simulation. If the transition probability $w(i \rightarrow f)$ is greater than the chosen random number, the new configuration σ_f is accepted. If $w(i \rightarrow f)$ is less than the random number, the previous configuration σ_f is kept.

Once converged, the metropolis algorithm guarantees that the configurations sampled in a Monte Carlo simulation occur with a frequency given by the probability distribution function (eqn. (2.7)). Hence, thermodynamic averages such as the average enthalpy can be obtained as simple arithmetic averages over the sampled configurations. Within a Monte Carlo simulation, the position of the lattice sites of a finite sized crystal are stored in memory with periodic boundary conditions and the enthalpy of the sampled configurations are calculated with a cluster expansion. We can distinguish between two types of simulations: (i) cooling or heating simulations at constant μ and (ii) simulations in which the chemical potential is varied at constant temperature (T). At fixed T and μ, a large number of configurations are sampled with the metropolis algorithm. A Monte Carlo step has passed once every Mn site in the Monte Carlo cell has been queried on average once. Typically on the order of 1000-10,000 MC steps are required to obtain convergence and the first several hundred to a thousand MC steps are omitted from the averaging as these initial states are not representative of the equilibrium. As the external thermodynamic variables (i.e. T and μ) are varied, the starting configuration of the Markov chain under the new conditions is often taken to be the final configuration at the previous external conditions.

2.4 Elastic Band Method

In the present work, we have used the elastic band method to calculate the activation energy barrier for proton diffusion in various $MnOOH_x$ polymorphs. The elastic band method enables the determination of the minimum energy path between two energetically stable end-points [33]. The method starts with a discretized path of, on the order of, 4-8 replicas of the system that are intermediate between the initial and final states of the path. The replicas are obtained by linear interpolation. A global energy minimization, using the First Principles calculations mentioned above, is then performed with respect to ionic positions in each replica whereby the coordinates of each replica are connected to those of its neighboring replica in the interpolation sequence by a string. The working of the algorithm can be compared to the tightening of an elastic band across a saddle point between two minima of the energy landscape.

The elastic band method is restricted to calculations in systems that are characterized by a periodic cell. To calculate activation barriers with this method, therefore, it is necessary to work with periodic $MnOOH_x$ supercells that are large enough to minimize the interaction between the periodic images of the proton in the activated state.

2.5 Molecular Dynamics

Molecular Dynamics (MD) simulation was employed to determine the location of protons and estimate the diffusion path for protons in ramsdellite. The MD simulation used in this work was a quick, approximate method to obtain qualitative results; accurate calculations to determine the proton location and diffusion path have been performed using First Principles calculations, as described later. The MnO_2 framework of ramsdellite was held to be immobile during the MD simulation. The Mn-H interaction

was modeled using long-range electrostatic interactions. The O-H interaction is modeled using an attractive Morse potential

$$V(O\text{-}H) = D[1-\exp(-\beta(r-r_o))]^2 \qquad (2.12)$$

until a cutoff of 1.5 Å. Beyond that, the O-H interaction is modeled using electrostatic interactions. The parameters for the Morse potential, which were developed by Saul et al. [34] using *ab initio* quantum mechanical cluster calculations, are presented in Table 1. Proton diffusion has been experimentally calculated to be very slow in MnO_2 [35] and therefore, the MD simulation was carried out at T=3500 K to speed up the diffusion process. More details about Molecular Dynamics simulations can be found in Ref. [36].

Chapter 3

Structure of MnO_2

3.1 Introduction

About 200,000 metric tons of γ-MnO_2 is used annually as cathode material in alkaline cells [37], and significant effort is expended in a continual attempt to optimize and improve the material.

Based on the method of production, γ-MnO_2 can be categorized into Natural manganese dioxides (NMD), Chemical manganese dioxides (CMD) and Electrolytic manganese dioxides (EMD). The γ-MnO_2 polymorph does not denote a unique structure but has been suggested to be either a single phase with considerable disorder [38] or a multi-phase assembly [39]. All of the relevant phases of MnO_2 in this study consist of a hexagonal close packed lattice of oxygen ions with Mn cations occupying half the octahedral sites. A number of different names have been given to specific arrangements of the Mn atoms in such a close-packed oxygen framework, of which pyrolusite (β-MnO_2) is generally regarded as the most stable structure [38]. Pyrolusite is the densest polymorph of manganese dioxide and has the rutile structure [38]. The structure may be described as infinite single chains of edge-sharing manganese octahedra, which are connected by corners to other single chains as shown in Figure 3.1 a). This sort of arrangement leads to formation of a tunnel structure and pyrolusite is said to contain 1×1 tunnels.

In addition to pyrolusite, γ-MnO_2 has been claimed to contain ramsdellite (R-MnO_2), ε-MnO_2 and other polymorphs. Ramsdellite is closely related to the pyrolusite

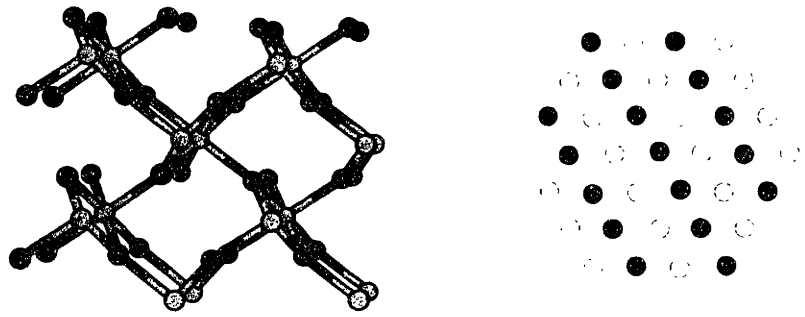

a)

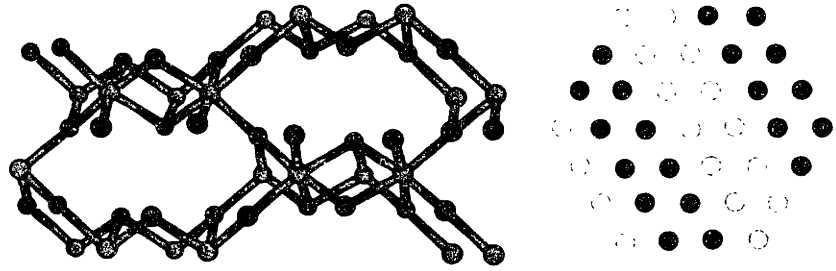

b)

Figure 3.1: Schematic representation of the structure of a) pyrolusite and b) ramsdellite: usual representation (left) and lattice gas representation of the cationic lattice (right). In the former representation, light and dark circles represent Mn and oxygen atoms respectively. The latter representation shows the basal plane of the hexagonal close packed structure. In the latter representation, only Mn atoms (represented by filled circles) and vacant octahedral sites (represented by empty circles) are represented.

structure except that the single chains of edge-sharing octahedra are now replaced by double chains, as shown in Figure 3.1 b). The ramsdellite structure is said to contain 1×2 tunnels. Highly textured fibrous samples of manganese dioxide that are prepared electrochemically are designated as ε-MnO_2. This structure has been described by De Wolff et al [40] as a hexagonal closed packing of O^{2-} with Mn^{4+} stochastically distributed over half the available octahedral interstices (similar to the NiAs structure), though more recently, ordered versions of ε-MnO_2 have also been proposed [39].

The γ-MnO_2 polymorph is a highly disordered material. The disorder in γ-MnO_2, which broadens and leads to selective extinction of certain X-ray diffraction reflections [38], is thought to be due to a variety of structural features. Below, we give a brief description of each of the various structural models that have been proposed to explain the structural complexity in γ-MnO_2.

Based on x-ray diffraction patterns, De Wolff [41] first proposed that γ-MnO_2 is a random intergrowth of the pyrolusite and ramsdellite structures. The boundary between the two units is thereby referred to as the De Wolff defect.

Chabre and Pannetier [38] used a XRD simulation package (DIFFAX) to show that while De Wolff disorder is supported by several experimental observations (HRTEM images, shift of X-ray diffraction lines), it cannot account for many features of the X-ray diffraction data of γ-MnO_2. In particular, it cannot explain the characteristically broad and diffuse diffraction peaks in γ-MnO_2. To explain the broad nature of the diffusion peaks, they introduced the additional concept of microtwinning. Figure 3.2 shows microtwinning in ramsdellite [38]. The figure shows that microtwinning generates new local environments for manganese ions located in the twinning plane. In the ideal ramsdellite structure, each Mn^{4+} ion has 4 in-plane nearest neighbor Mn^{4+} ions. In the

twinned structure, this unique configuration is replaced by some of the Mn^{4+} ions having 5 in-plane nearest neighbor ions. Chabre and Pannetier claim that the formation of a twin

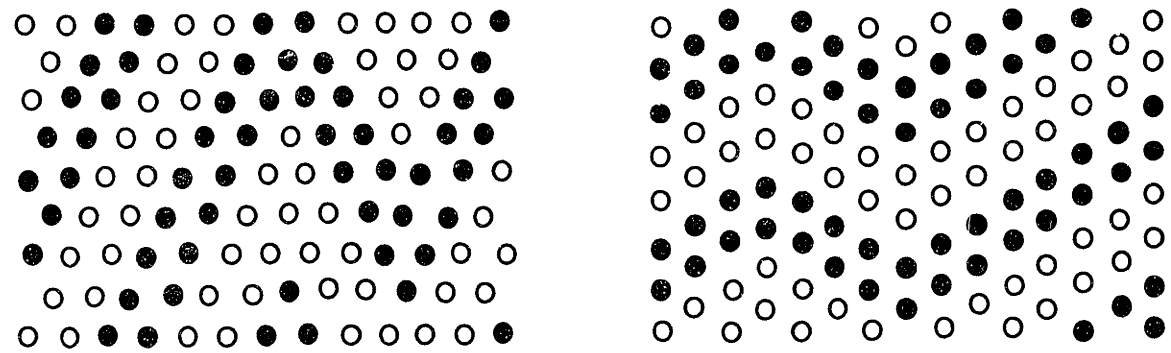

a) b)

Figure 3.2: Microtwinning of an ideal ramsdellite lattice on a) [021] plane and b) [061] plane. (filled circles: Mn^{4+} at z=1/2; open circles: Mn^{4+} at z=0). Coordinate z is along the c-axis, perpendicular to the basal plane.

becomes favorable in the presence of either Mn^{3+} ions or Mn vacancies [38]. The XRD patterns obtained by incorporating both De Wolff disorder and microtwinning closely match those obtained from experiments and hence Chabre and Pannetier classified all possible γ-MnO_2 structures with two variables: % De Wolff disorder and % microtwinning.

Anderson et al. [42] developed a Rietveld refinement model to explain the characteristics of the XRD patterns for a wide variety of EMD (Electrolytic manganese dioxide) samples. In contrast to Chabre and Pannetier, who disregard ε-MnO_2 as a component of EMD, Anderson et al. incorporate it as one of the possible phases in the rietveld model. Their model describes EMD as a binary mixture of ε-MnO_2 and

pyrolusite-ramsdellite intergrowth (which they call γ-MnO_2) crystallites with different crystallite domain sizes. In agreement with Chabre and Pannetier, their model incorporates microtwinning and De Wolff disorder in the intergrowth phase.

The microstructure and crystallography of EMD was studied by Heuer et al., [39] using transmission electron microscopy (TEM). In contrast to previous TEM studies of EMD that used powder prepared from bulk material by grinding [43], Heuer et al. used TEM thin foils that were prepared from bulk EMD by ion beam milling. Based on the TEM data, they described EMD as a heterogeneous phase system, partially consistent with Anderson's results. They found that the overall material contains ~50% Ramsdellite, ~30% ε-MnO_2 and ~15% Pyrolusite. They also believe that Mn-vacancy ordering is present in ε-MnO_2 (in accordance with De Wolff et. al [40]) and suggest a model for a fully ordered form of ε-MnO_2, which they call ε'-MnO_2 (as shown in Figure 3.3). However, no evidence for microtwinning was found in their EMD samples.

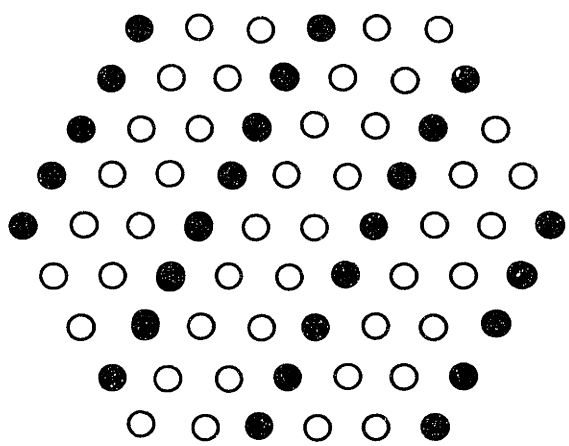

Figure 3.3: Ordering of Mn atoms in ε'-MnO_2. Filled and empty circles represent Mn atoms and vacancies respectively. Only one basal plane is shown, but the adjacent basal plane can be found by interchanging Mn atoms and vacancies.

Bowden and Hackney [44] provided an alternative interpretation of the γ-MnO_2 structure. They performed convergent beam electron diffraction (CBED) experiments on EMD powder. The CBED patterns revealed streaks of intensity in the reciprocal space, which they interpret to be resulting from two-dimensional sheets of scattered intensity perpendicular to the c-axis ([001] direction). Traditionally, sheets of intensity in reciprocal space have been interpreted in terms of *linear disorder* [45]. This disorder can be considered as a displacement of the atomic positions from a periodic structure in all but one direction. The structural model consistent with such linear disorder is one where Mn ions are pseudo-randomly distributed over the octahedral sites, but with the restriction that no face-sharing octahedra are occupied simultaneously. Since octahedra connect by faces along the direction parallel to the ABAB oxygen stacking (hereafter referred to as the c-axis), this leads to perfectly ordered Mn-vacancy chains along the c-axis. This can be thought of as a version of the NiAs structure but with substantial short-range order along the c-axis. The results of Bowden and Hackney are consistent with those of Chabre and Pannetier since the combination of De Wolff defects and extensive twin defects produces the *linear disorder* that result in the observed sheets of intensity in reciprocal space. To summarize, their results indicate that EMD consists of randomly oriented homogeneous ramsdellite crystallites distorted by the presence of one-dimensional pyrolusite defects and extensive twin defects.

In the present chapter, we demonstrate the use of computational methods to investigate the polymorphs of γ-MnO_2 and try to understand the reasons for its structural complexity.

Section 3.2 deals with the use of lattice models in determining the relative stability of various MnO_2 polymorphs. The 2-Dimensional ground state map obtained from earlier studies, is also reviewed.

In section 3.3, the energetics of the MnO_2 system is reviewed. We identify the dominant interactions in the system and introduce the low energy structures for this system.

Section 3.4 deals with the thermodynamic properties of the system. Monte-Carlo simulations have been used to identify the ground state, nature of excitations and the transition temperature for Mn-vacancy disorder in MnO_2.

The effect of defects on the structural stability of γ-MnO_2 is investigated in Section 3.5 and section 3.6 offers a summary of our results on the structure of γ-MnO_2.

3.2 Lattice Models

As mentioned earlier, γ-MnO_2 can be thought of as consisting of a (possibly distorted) hexagonal close packed (hcp) oxygen framework with Mn and Vacancies each occupying half of the hcp lattice's octahedral sites. The hcp octahedral sites can be shown to form a simple hexagonal lattice themselves and all the MnO_2 polymorphs relevant to γ-MnO_2 can be understood as different Mn-Vacancy arrangements on this hexagonal lattice. There are many other MnO_2 polymorphs (e.g., those based on a face centered cubic lattice of oxygen) but these do not seem to appear in the γ-MnO_2 materials. Hence, the problem of understanding MnO_2 structures can be formally approached by investigating the ordered states of a binary alloy (Mn and Vacancies are the constituents) on a simple hexagonal lattice.

3.2.1 The 2D Picture

A common feature to almost all of the important MnO_2 structures is that Mn atoms never simultaneously occupy two sites in adjacent hexagonal planes that differ only by a displacement along the c-axis. This is simply because these sites are quite close

together and there is a large electrostatic repulsion between the Mn^{4+} cations. However, this constraint provides a great simplification because knowledge of the Mn arrangement in a single hexagonal plane immediately tells us the occupations of all the other planes. The occupations of an adjacent plane is determined by switching all the Mn occupied sites to Vacancies and all the Vacancy occupied sites to Mn. Therefore, the problem of characterizing the Mn-vacancy configuration can be reduced to considering only a single hexagonal plane.

Lattice models can be quite useful for understanding the possible Mn-vacancy arrangements on a simple hexagonal plane. Chabre and Pannetier [38] have constructed a ground state map showing the region of stability for several of the known MnO_2 polymorphs (Figure 3.4). Only the first three pair interactions between Mn sites were assumed non-zero in this model. Earlier, Kanamori and Kaburagi [46] computed a complete ground state map for the first three pair interactions on a hexagonal lattice. This map, shown in Figure 3.5, displays all the structures that can be stable when varying the interactions. Note that it contains several structures not included in the ground state map of Chabre and Pannetier. Pictures for each of the different structures in the ground state map as well as a few others, represented by the occupations of a single hexagonal plane, are shown in Figure 3.6.

The 2D picture is a convenient way to represent the structures and identifies most of the MnO_2 polymorphs using only 3 interactions and only 2 dimensions. However, the 2D picture does not accurately model the Mn-vacancy thermodynamics in MnO_2. Even though Figure 3.5 identifies most of the key structures, it does not explain the simultaneous presence of these phases in γ-MnO_2. The structures on a ground state map are mutually exclusive in equilibrium and hence the ground state map in fact suggests that the different phases should not be simultaneously present in γ-MnO_2.

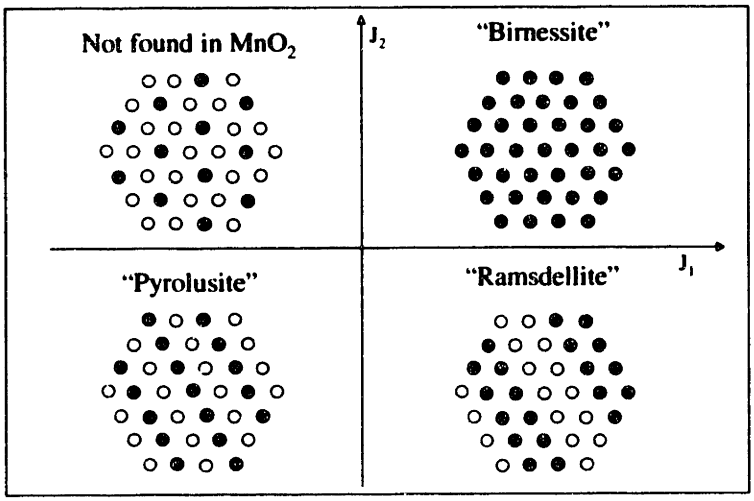

Figure 3.4: The ground state map for the first three nearest-neighbor pair interactions on a hexagonal plane (adapted from Chabre and Pannetier [38]). The map corresponds to $J_3 < 0$. The lattices represent the structures stable in the different parts of the plane (Filled and empty circles denote Mn and vacancies respectively).

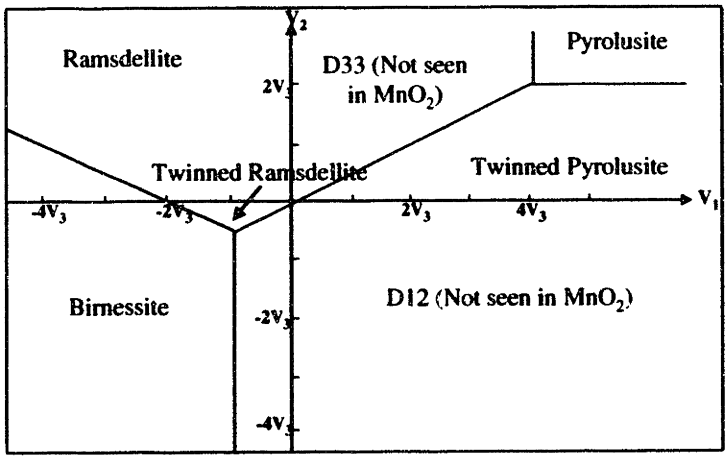

Figure 3.5: The complete ground state map for the first three nearest-neighbor interactions on a hexagonal plane (adapted from Kaburagi and Kanamori [46]).

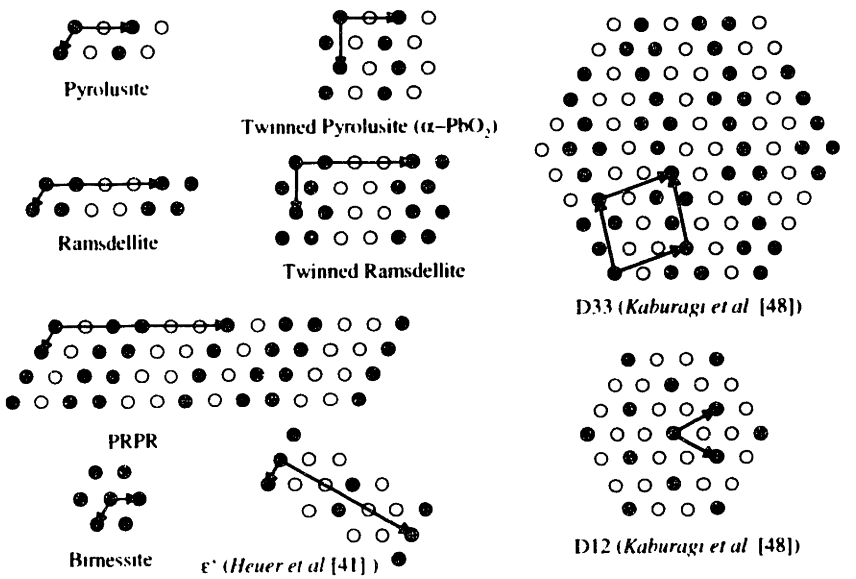

Figure 3.6: The unit cells for important polymorphs of MnO_2. Filled and empty circles represent Mn and vacancies respectively.

Furthermore, the 2D model considers only in-plane interactions and thereby assumes that the structure energetic/thermodynamics can be reduced to a 2D lattice model. However, as we show later, the out-of-plane interactions matter a lot in determining the relative stability of structures. Hence, in order to understand the structural complexity of this material, the 2D model needs to be generalized. This can be accomplished with the cluster expansion formalism, described in section 2.2.1.

3.3 Cluster Expansion

In this section, the cluster expansion formalism has been used to identify the stable MnO_2 polymorphs and to understand the structural complexity in MnO_2.

3.3.1 Fitting Procedure

Cluster expansion involves fitting the ECIs in eqn. (3) with the energies of known structures. For the present work, the energies of all structures were initially calculated with a ferromagnetic arrangement. The various clusters involved in this calculation are shown in Figures 3.7, 3.8. In addition to a constant, 12 pair clusters and 3 quadruplet clusters were used for the ferromagnetic fit. Since MnO_2 has 50% Mn atoms and 50 % vacancies, all the three-point interactions reduce to zero and hence no such terms were included in the fit. For the ferromagnetic fit, 36 structural energies were used to fit 16 ECIs. The cross-validation method was also used to optimize the quality of the fit [25]. Interactions based on ferromagnetic energies are shown in Figure 3.9. However, MnO_2 is paramagnetic at room temperature [47] and hence it is more accurate to use paramagnetic energies in the fit. The energy of a paramagnetic spin configuration cannot be directly obtained from the First-Principles methods used in this work. Hence, in order to obtain the paramagnetic energy of a structure, the energy of the structure is calculated with various magnetic arrangements, and these energies (relative to ferromagnetic energy) are then fit to a Heisenberg Hamiltonian. The constant term of this fit gives the difference between the paramagnetic and ferromagnetic energies of the particular Mn-vacancy arrangement (ΔE). An example of this magnetic cluster expansion fit is shown in Table 3.1, which gives values for the magnetic interactions in a few MnO_2 polymorphs. The table shows that magnetic interaction can vary significantly, depending upon the Mn-vacancy configuration.

Typically, 20 different magnetic arrangements were computed for a given Mn-vacancy arrangement and the whole procedure was repeated for 16 structures. The first 4

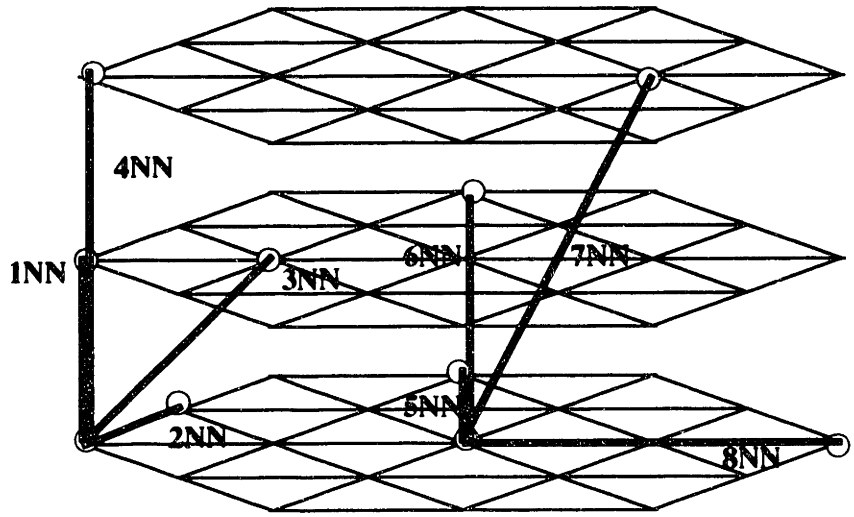

Figure 3.7: Illustration of the first eight nearest-neighbor pairs on a hexagonal lattice.

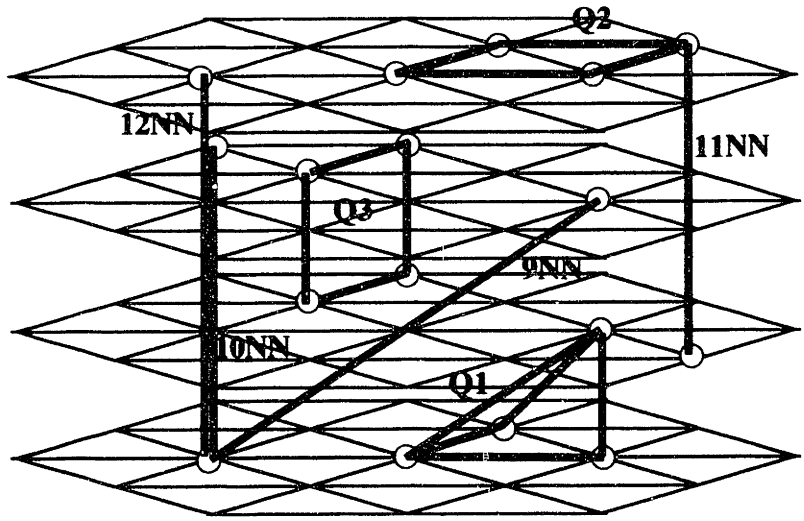

Figure 3.8: Illustration of 9th to 12th nearest-neighbor pairs and select quadruplets on a hexagonal lattice.

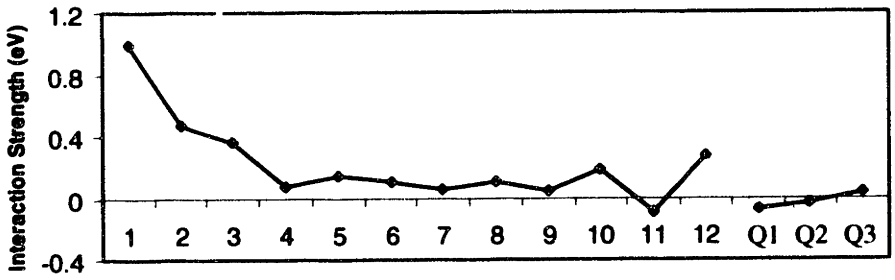

Figure 3.9: The strength of the Mn-vacancy effective cluster interactions (ECI) based on ferromagnetic energies.

Clusters	Birnessite	ε'-MnO_2	Rams	Pyro
Constant (ΔE)	1.625	-41.7	-42.23	-67.18
1NN	-	-	-	-
2NN	-4.5	2.8	3.75	15.4
3NN	-	12.6	18.7	9.5
4NN	0.1	2.6	3.4	3.45
5NN	-0.4	3.2	0	

Table 3.1: Magnetic cluster expansion fit for various MnO_2 polymorphs. The constant term in the fit indicates the difference between paramagnetic and ferromagnetic energies (ΔE) for the structure.

pair clusters in the Mn-vacancy cluster expansion were then fit to the difference between the paramagnetic and ferromagnetic energies (ΔE) of these 16 structures. The strength of the interactions for this paramagnetic energy correction is shown in Figure 3.10. To obtain the paramagnetic interactions for this system, the paramagnetic-correction interactions need to be added to the ferromagnetic interactions. The strengths of these total interactions describing the paramagnetic energy are shown in Figure 3.11. Table 3.2 gives the values for the various cluster interactions.

The accuracy of the Mn-Vacancy ferromagnetic cluster expansion can be observed from Figure 3.12. In this figure, the calculated ab-initio ferromagnetic energy is compared with the *excluded prediction* energy for each structure. In order to obtain the excluded prediction energy for a particular structure, the energy of that structure is excluded while fitting the interactions, and then the energy of the structure is calculated from the resultant fit. By comparing the two energies, we get an estimate of the predictive power of the fit. Only low-energy structures, that have an energy difference less than 500 meV per formula unit, are included in the figure. The structures are arranged in increasing order of their energies. In addition, the energy of pyrolusite (numbered 1 in the figure) has been renormalized to zero. As can be observed, the magnitude of the average predicted error for these structures is only about 0.026 eV while the energy scale spanned by these MnO_2 polymorphs is about 0.5 eV. The errors are actually lower for the key low-energy MnO_2 structures (numbered from 1 to 8). The errors for the complete ferromagnetic fit are shown in Table 3.3. The table also gives an estimate of the errors for the paramagnetic and magnetic cluster expansion fit.

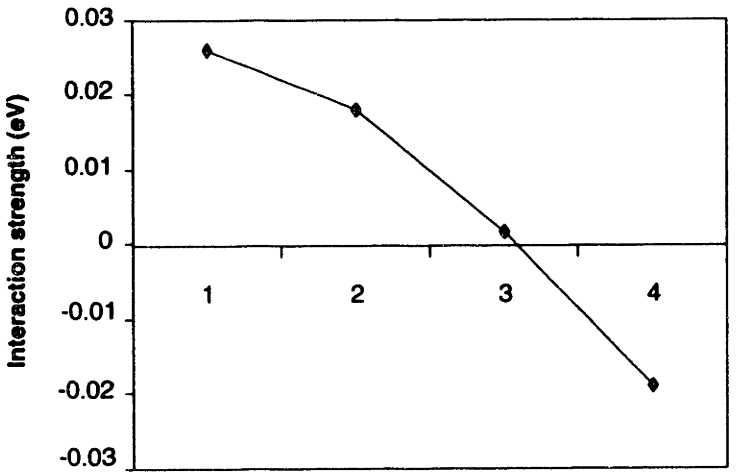

Figure 3.10: The strength of the effective cluster interactions that represent the energy difference between the paramagnetic and ferromagnetic state.

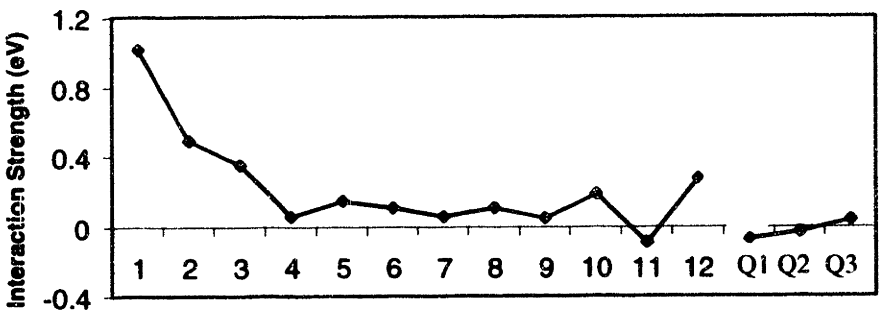

Figure 3.11: The strength of the net effective cluster interactions (ECI) for MnO_2 based on paramagnetic energies.

Cluster	Multiplicity	Ferro ECI (eV)	Para Corrn. (eV)	Total ECI (eV)
Const.	1	-45.927	0.005	-45.922
1NN	2	0.988	0.026	1.014
2NN	6	0.470	0.019	0.489
3NN	12	0.356	0.002	0.358
4NN	2	0.069	-0.019	0.050
5NN	6	0.147	-	0.147
6NN	12	0.104	-	0.104
7NN	12	0.053	-	0.053
8NN	6	0.108	-	0.108
9NN	12	0.044	-	0.044
10NN	6	0.181	-	0.181
11NN	6	-0.099	-	-0.099
12NN	2	0.276	-	0.276
1QQ	12	-0.069	-	-0.069
2QQ	6	-0.029	-	-0.029
3QQ	12	0.034	-	0.034

Table 3.2: Values for the various effective cluster interactions (ECI) in MnO_2. The multiplicity for each cluster is shown in the table.

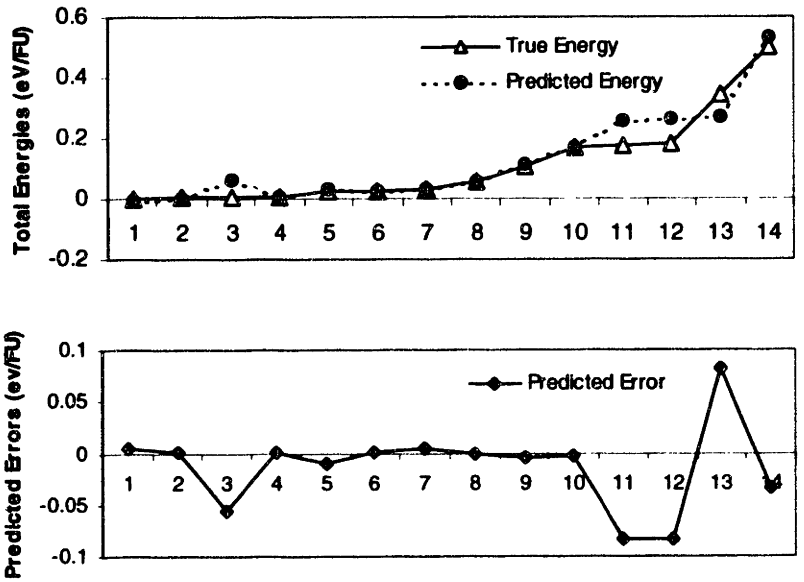

Figure 3.12: Accuracy of the MnO_2 Mn-vacancy Cluster Expansion for ferromagnetic energies. The key MnO_2 polymorphs are numbered from 1-8. Energy of pyrolusite is taken as zero of energy.

Fit	rms error (meV)	Predicted error (meV)
Ferromagnetic fit	56.63	118.2
Paramagnetic fit	11.35	19.76
Magnetic Cluster Expansion	0.43	2.9

Table 3.3: Accuracy of the MnO_2 cluster expansion fit for ferromagnetic energies, paramagnetic energies and magnetic interactions for a Mn-vacancy arrangement.

3.3.2 Discussion

Table 3.4 shows the energy as computed with GGA for a large number of MnO_2 arrangements. In each case, the energy is referenced to that of pyrolusite. The well-known arrangements are listed by name, whereas the other ones are numbered, but can be identified from the correlations. Pictures of all the following structures can be found in Figure 3.6. Pyrolusite and ramsdellite are well known. The ε' structure is the one recently proposed by Heuer [39] in EMD. Arrangements denoted by α-PbO_2 and Tw-R represents fully twinned pyrolusite and fully twinned ramsdellite respectively [38]. PRPR consists of alternate ramsdellite and pyrolusite building blocks. The D33 structure is a possible ground state of the 2D hexagonal lattice that was identified in the ground state study of Kanamori and Kaburagi [46] as lying between pyrolusite and ramsdellite in interaction space. Birnessite is the mineral in which manganese fully occupies alternating layers of octahedral sites perpendicular to the c-axis of the hcp oxygen stacking. From the calculated energies one can see that these structures make up most of the low energy arrangements, thereby giving an indication of why they may be most common in nature. Most other arrangements that were made by us have higher energy. Magnetism plays a key role in the relative stability of the low-lying structures. For a ferromagnetic spin arrangement, the ε' structure is actually the ground state among all the structures that we considered, which does not seem to agree with the experimental observation that pyrolusite is the most stable form of MnO_2. Pyrolusite is recovered as the ground state in the paramagnetic computation. The MnO_2 systems are antiferromagnetic at low temperature [47] and paramagnetic at room temperature. Similarly, pyrolusite becomes more stable than ramsdellite upon going from ferromagnetic to paramagnetic energies. The paramagnetic energy correction has ECI, which are mainly positive, making the total ECI slightly more repulsive (i.e. Mn-Mn repulsive or Mn-vacancy attractive) than for the

Name	Ferro Energy (meV/F.U)	Para Energy (meV/F.U)	1NN	2NN	3NN	4NN	5NN	6NN
Pyrolusite	0	0	-1	-.33	.33	1	-.33	.33
Ramsdellite	-0.003	0.022	-1	.33	-.33	1	-.33	.33
ε-prime	-0.009	0.016	-1	.11	-.11	1	-.33	.33
α-PbO2	0.013	0.037	-1	-.33	.33	1	.33	-.33
Tw-R	0.047	-	-1	.33	-.33	1	0	0
PRPR	-0.005	-	-1	.11	-.11	1	-.33	.33
D33	0.018	0.040	-1	0	0	1	-.33	.33
Birn	0.096	0.162	-1	1	-1	1	1	-1
1	0.025	0.079	-1	.33	-.33	1	0	0
2	0.158		-1	0	0	1	.33	-.33
3	0.166	0.157	-1	-.33	.33	1	1	-1
4	0.171	0.201	-1	0	0	1	0	0
5	0.204	0.252	-.33	-.33	0	-.33	1	-.33
6	0.301		-.50	0	-.16	0	.33	-.16
7	0.338		-.50	0	-.16	0	0	-.16
8	0.354	0.407	.33	-.33	-.33	-.33	1	.33
9	0.371		0	0	-.33	1	.33	-.33
10	0.373		0	0	-.33	1	.33	0
11	0.541		0	-.33	0	0	0	0
12	0.594	0.663	0	-.33	0	-1	-.33	0
13	0.602		0	0	-.33	0	0	-.33
14	0.644	-	.33	.11	-.11	-.33	.55	-.33
15	0.681		-.50	.33	-.16	0	-.33	.16
16	0.697		0	0	0	-.50	-.33	0
17	0.715	0.763	-.33	.11	-.11	-.33	-.33	0
18	0.792	0.826	.33	-.33	-.33	1	1	.33
19	1.008		0	0	0	1	-.33	0
20	1.029	-	0	.33	-.33	1	0	-.33
21	1.138		0	.33	-.16	0	0	-.33
22	1.227		0	.33	0	1	-.33	0
23	1.232	-	0	.33	0	1	0	-.33
24	1.236	1.286	.33	.11	-.11	1	-.33	-.33
25	1.387	-	-.50	1	-.50	0	1	-.50
26	1.481	1.551	1	-.33	-.33	1	-.33	-.33
27	1.489		-.50	.33	-.33	0	0	-.16
28	1.805	-	-.33	1	-.33	-.33	1	-.33

Table 3.4: Pair correlations and energies for 36 MnO_2 polymorphs. The key structures are named while the other structures are numbered in increasing order of their energies. All energies are relative to the energy of pyrolusite. The second and third columns list the energy obtained for ferromagnetic and paramagnetic Mn-Mn spin arrangements respectively.

purely ferromagnetic ECI. The fact that Mn ions repel each other slightly less in the ferromagnetic state than in the paramagnetic state (as parameterized by various AF arrangements) may be because ferromagnetic spin order leads to more Mn-Mn hopping and hence, reduce the electrostatic repulsion. Antiferromagnetism reduces electron hopping as an electron has to pay the exchange penalty when going from a Mn ion with given spin to one with opposite spin. Hence, paramagnetic and antiferromagnetic spin states lead to higher repulsion among Mn ions. In this material, this effect changes the groundstate from ε'-MnO_2 (with high number of nearest neighbor Mn ions) to pyrolusite (with less Mn-Mn nearest neighbors). These results therefore stress the importance of properly treating the magnetic state when performing computations on Mn oxides [24]. Very often spin polarized computations are reported with ferromagnetic spins as this leads to a unit cell which is the same as the one determined by the ions. Clearly, as in the case of Mn^{3+} ions [24], this would give incorrect results for the relative stability of the different Mn arrangements.

Note that the ε' structure, proposed by Heuer and Hughes [39] based on XRD and TEM diffraction, is also very low in energy. This structure is a fully vacancy ordered version of ε-MnO_2, in which the hcp oxygen sublattice of NiAs is maintained but in which certain cation sites in NiAs are either fully occupied by Mn^{4+} cations or are vacant.

Several of the MnO_2 structures have very similar energy, often different by less than the thermal energy at room temperature. One might therefore expect significant disorder in a real MnO_2 material. Below we show that this argument needs to be made more carefully and that while *defect-induced* disorder may exist, pyrolusite has no *equilibrium* thermal disorder at temperatures below ≈3000 K. The close energy of many of the structures seems at odds with the large values for the ECI. The first three effective pair interactions in Figure 3.11 are all above 300 meV, with the nearest neighbor one

being more than 1 eV. Part of the close energy competition between various structures arises because of the geometric frustration between these first three interactions. V_1 points between an octahedral site and the octahedral site directly above it (in the direction of the c-axis). V_2 is the nearest neighbor in the hexagonal plane of octahedral sites perpendicular to the c-axis (Figure 3.13) and the vector defining V_3 is the sum of the vectors of V_1 and V_2. Together these three interactions form a triangle along which only repulsive interactions exist. Since it is not possible to organize Mn and vacancies on the vertices of a triangle so that all edges are Mn-Vacancy edges, the system is referred to as frustrated. This implies that at least one of the first three pair interactions is always "unsatisfied", i.e. it has a Mn-Mn bond, which gives a high energy due to the repulsive interaction. It is in part this frustration, which leads to the large number of structures with close energies. Pyrolusite and ramsdellite can be seen as two different answers to this frustration (Figures 3.13, 3.14). In pyrolusite, more in-plane nearest neighbor bonds (V_2) are Mn-vacancy, but less V_3 interactions are satisfied than in ramsdellite. This can be seen from the correlations for these two structures in Table 3.3. The second neighbor correlation for pyrolusite is $-1/3$, implying that it has more unlike nearest neighbor bonds in the plane than ramsdellite, with a correlation of $+1/3$. The opposite holds true for the V_3-correlations, the values being $+1/3$ and $-1/3$ for pyrolusite and ramsdellite respectively. All low energy structures have a nearest neighbor correlation (V_1) that is -1, implying that always having vacancies stack on top of Mn along the c-axis is a requirement for low energy. The c-axis ordering makes sense since the nearest neighbor sites along the c-axis share an octahedral face and separate each other by only ≈ 2.40 Å for most of the MnO_2 polymorphs.

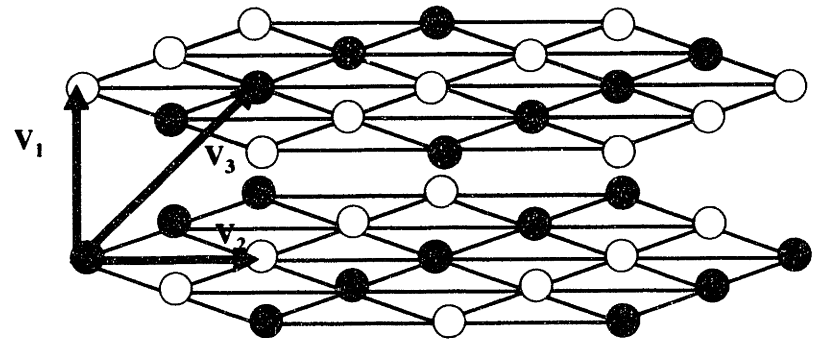

Figure 3.13: Frustration in Pyrolusite. The first three nearest-neighbor interactions are shown in the figure. Filled and empty circles represent Mn and vacancies respectively.

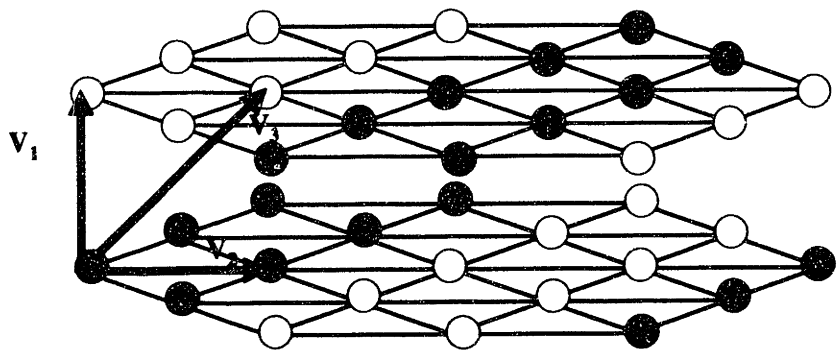

Figure 3.14: Frustration in Ramsdellite. The first three nearest-neighbor interactions are shown in the figure. Filled and empty circles represent Mn and vacancies respectively.

For those structures that always have perfect −1 correlation along the c-axis the three-dimensional interaction model can be renormalized to a two-dimensional one (since the configuration of Mn and vacancies in one plane fully characterizes the configuration

in any other plane, every 3-D interaction can be reduced to a corresponding 2-D interaction along the hexagonal plane). The renormalized interactions are shown in Figure 3.15. To limit confusion we have kept the same numbering scheme as in the 3D model. Hence, the interactions listed as "2NN" is the first neighbor interaction in a hexagonal plane. Figure 15 reveals the source of much of the near structural degeneracy in MnO_2. While the 3D interactions are strong, the renormalized effective 2D interactions are very small and frustrated. Hence, almost any configuration of Mn in the 2D plane, which preserves perfect c-axis correlation, will be low in energy. Clearly, this is the case for the low energy configurations in Table 3.3. The model presented by Chabre and Pannetier [38] is essentially this 2D renormalized interaction model.

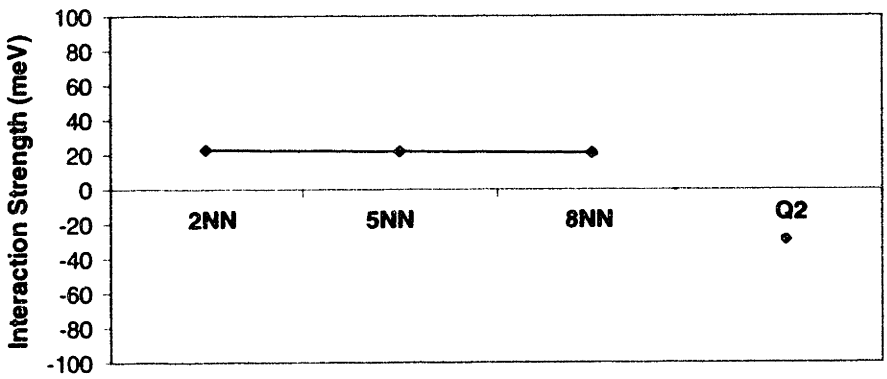

Figure 3.15: The strength of the two-dimensionally renormalized effective cluster interactions in MnO_2. The relevant clusters are shown in figures 3.7, 3.8.

We show below that while our model causes near structural degeneracy, it does not allow for thermal disorder at low temperature.

3.4 Mn-Vacancy thermodynamics

The finite temperature equilibration of the Mn-vacancy arrangement can be achieved using standard Monte Carlo techniques. Simulations were performed with a 10×10×10 supercell of the primitive hexagonal cell (2 lattice sites per cell) containing a total of 2000 lattice sites (consisting of equal number of Mn atoms and vacancies). The Hamiltonian in this Monte Carlo simulation is the cluster expansion of eqn. (2.5) with the paramagnetically corrected ECI of Figure 3.11. The number of Monte Carlo steps per site was in the range 2500-3000 for each temperature and of those, the first 1000 were excluded from calculations of thermodynamic quantities to allow for equilibration. More details about Monte Carlo simulation can be found in Ref. [27].

3.4.1 Monte-Carlo Results

Figure 16 shows the energy as function of temperature while figures 3.17, 3.18 show snapshots of the structure at various temperatures. Figure 3.16 indicates a first-order transition temperature from the ordered pyrolusite to a disordered state at about 10,000K.

Even though there are many structures with nearly the same energy, equilibrium Mn disorder only occurs at about 10,000K. This apparent disparity can be explained by considering the 3D nature of the material: While the 2D model as proposed by Chabre and Pannetier [38] is useful to understand the possible structures that may form, it is misleading for understanding thermal excitations. Every Mn in the 2D model actually corresponds to a perfect column of alternating Mn-vacancies along the c-axis. If we assume the c-axis correlation to be preserved, any perturbation of the 2D arrangement therefore corresponds to moving complete c-axis columns. Hence, the energy for such an

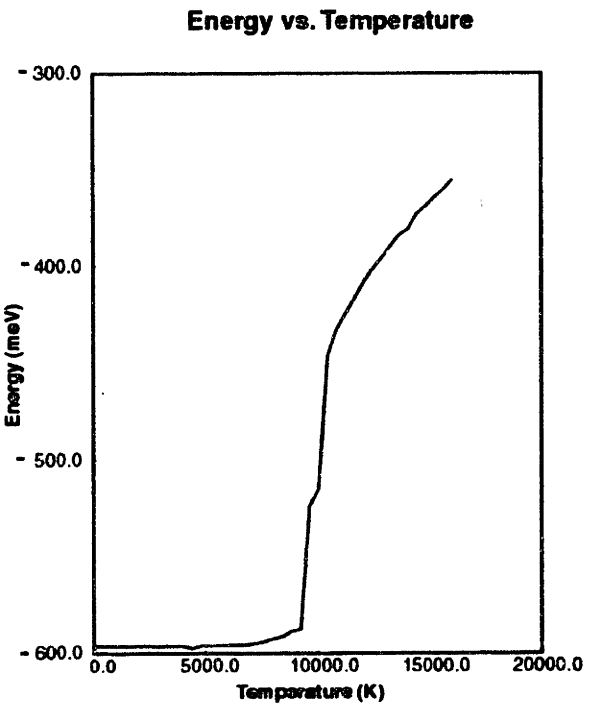

Figure 3.16: Graph of Energy as a function of Temperature for MnO_2 obtained from Monte Carlo simulations.

excitation will depend on the correlation length for ordering along the c-axis in the following way:

$$\Delta E_{exc} \propto \xi_c \Delta e \tag{3.1}$$

where Δe is the excitation energy in the 2D model and ξ_c is the correlation length along the c-axis. At low temperature ξ_c approaches infinity and there are no low-energy excitations in the system. Only when ξ_c becomes of the order of l do the 2D excitations become available. Hence, the order disorder temperature is largely determined by the c-axis correlation and the interaction in that direction. The strong V_1 interaction along the c-axis therefore sets the temperature scale for thermal disorder.

A similar phenomenon exists in $YBa_2Cu_3O_x$ where chains of oxygen atoms and vacancies order. The oxygen atoms and vacancies have very small interactions between

them but because of the length of the chains, the interaction *energy* between them is actually large [48]. The recent TEM and XRD observations by Hackney et al. [44] are consistent with these results. Even when disorder of Mn-vacancies exists in one hexagonal plane, long-range correlation exists along the c-axis, making this effectively a disorder of one-dimensional objects.

At room temperature, the theoretical equilibrium correlation length along the c-axis is likely to approach infinity. In a real material, the correlation length is limited by the grain size or the distance between defects. This brings up the possibility that the order/disorder temperature for Mn may be strongly influenced by the feature size of the MnO_2 crystals. In particular, in EMD, small domains or grains may limit the c-axis correlation length so that thermal disorder at relative low temperatures becomes possible.

Figure 3.17 is obtained on cooling and equilibrating the system from very high temperature to room temperature. The figure shows that pyrolusite is indeed the ground state of the system at room temperature. Figure 3.18 shows the system at ~3000K. This figure indicates that only at high temperatures can we observe thermal excitations in this system. These excitations do not form ramsdellite but instead seem to be more reminiscent of twin formation.

From Monte Carlo simulations, one can observe that pyrolusite is the equilibrium ground state at room temperature and that there are no low temperature thermal excitations for the system. Hence, if the system were governed only by equilibrium thermodynamics, γ-MnO_2 should contain only pyrolusite and only at high temperatures should we see disorder in the material. Therefore, the high disorder seen in real γ-MnO_2 at room temperature (ref. section 3.1) is not due to equilibrium thermodynamic disorder of MnO_2.

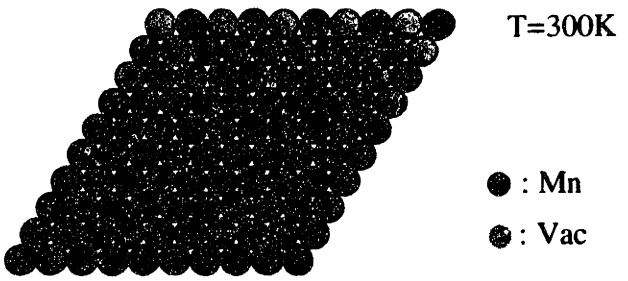

Figure 3.17: Snapshot of the cationic lattice obtained from Monte Carlo simulations at room temperature. Figure shows a basal plane of the hexagonal lattice. Dark and light circles represent Mn and vacancies respectively.

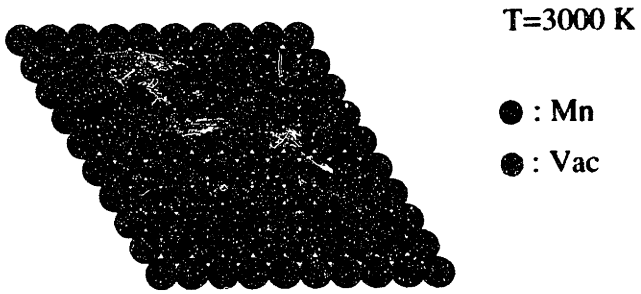

Figure 3.18: Snapshot of the cationic lattice obtained from Monte Carlo simulations at T=3000 K. Figure shows a basal plane of the hexagonal lattice. Dark and light circles represent Mn and vacancies respectively.

Defects could be a possible explanation for the structural complexity of γ-MnO_2 and hence calculations incorporating defects have been performed to study the effect of defects on the relative stability of various MnO_2 phases. The results, which are shown below, indicate that Ruetschi defects indeed introduce structural complexity in γ-MnO_2.

3.5 Effect of Proton compensated Mn deficiencies

EMD generally contains about 4 weight percent of structural water in the crystal structure, which influences not only electrochemical reactivity but also other properties, such as density, electronic conductivity and electrode potential [49, 50, 51]. Many studies have attempted to study the effect of structural water on the physical, chemical and electrochemical properties of EMD [52, 53]. At present, the cation vacancy model, proposed by Ruetschi [54], is the most successful model for explaining EMD properties. According to this model, γ-MnO_2 contains Mn vacancies. Each vacancy is coordinated to, and electrostatically compensated by, four protons. The protons are present in the form of OH^- ions, which replace the O^{2-} ions in the lattice without noticeable change in the lattice parameters. On the basis of this cation vacancy model, Ruetschi claimed that ramsdellite (R-MnO_2) is electrochemically much more reactive than pyrolusite (β-MnO_2) because ramsdellite contains Mn vacancies and a corresponding water content that provides an initial starting concentration of protons, which are useful for proton transfer. In contrast, pyrolusite contains almost no vacancies and thus very little water.

First Principles Calculations have been performed to ascertain the geometry and structural stability of Ruetschi defects in pyrolusite and ramsdellite. Monte Carlo simulations incorporating Ruetschi defects have also been performed to investigate the effect of Ruetschi defects on the structural stability of MnO_2.

3.5.1 Geometry and Energetics

Calculations were performed on pyrolusite and ramsdellite with a single Mn vacancy. The cells used for the calculations contained eight formula units so that the concentration of vacancies is 0.125. Initially, equilibration was attempted with H ions pointing towards the Mn vacancy. However, on relaxation, the H atoms evolve to lie along the edge of the [MnO_6] octahedra for pyrolusite as shown in Figure 3.19.

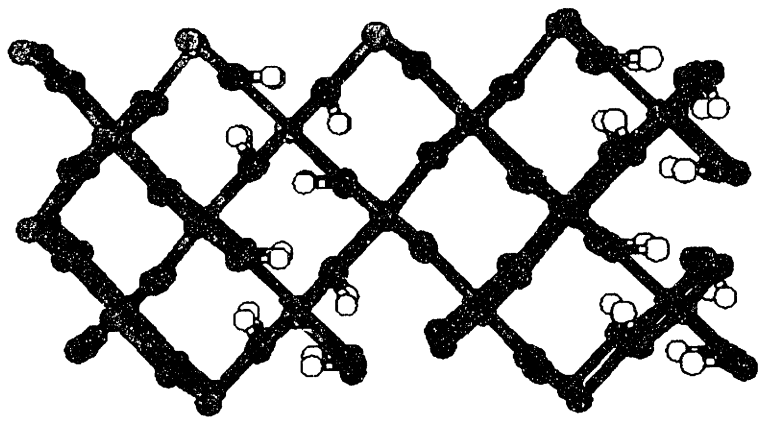

Figure 3.19: Geometry of Ruetschi defects in pyrolusite. Light and dark circles represent Mn and Oxygen atoms respectively. × indicate Mn vacancies while empty circles represent H atoms.

Similar calculations were performed in Ramsdellite with the same initial positions. However, the final position is slightly different in Ramsdellite compared to Pyrolusite. This is because Ramsdellite has a Mn atom near the Mn vacancy while Pyrolusite does not have the same feature. Hence, in Ramsdellite, the proton near the Mn atom points towards an oxygen atom further away from the Mn atom as can be seen from Figure 3.20.

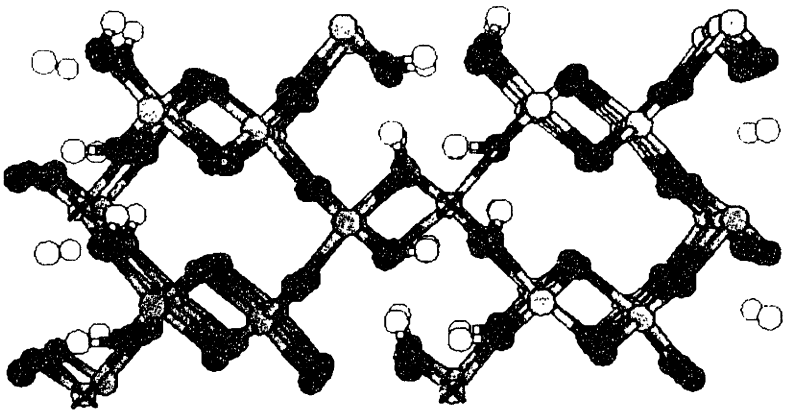

Figure 3.20: Geometry of Ruetschi defects in ramsdellite. Light and dark circles represent Mn and Oxygen atoms respectively. × indicate Mn vacancies while empty circles represent H atoms.

The effect of Ruetschi defects on the structural energies can be seen from Figure 3.21. The energy of pyrolusite has been normalized to zero so that the energy of ramsdellite can be compared with respect to pyrolusite. The plot shows that without Ruetschi defects, ramsdellite is slightly higher in energy as compared to pyrolusite. However, with a Ruetschi defect concentration of 0.125, the energy of ramsdellite per formula unit is ≈ 40 meV lower than that of pyrolusite. Thus, ramsdellite is clearly stabilized by Ruetschi defects.

While the concentration of defects is quite high in the calculation (1 out of every 8 Mn), it is likely that this stabilization of ramsdellite over pyrolusite remains present at lower defect levels. Linearly interpolating between the energies at zero and 0.125 defect concentration would indicate that ramsdellite is already stabilized over pyrolusite at 1.5 % concentration of Ruetschi defects (see Figure 3.21).

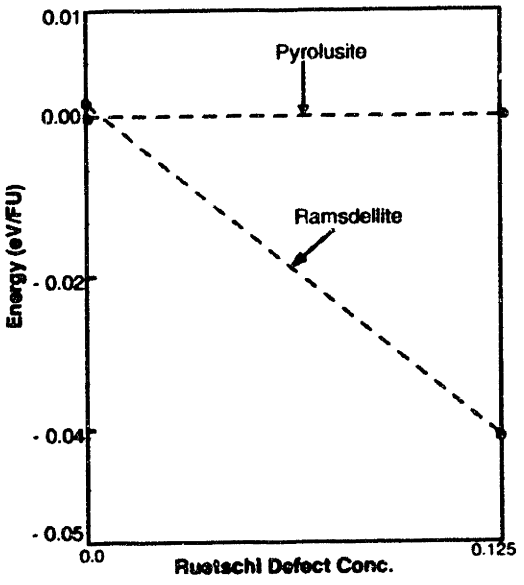

Figure 3.21: Effect of Ruetschi defects on the structural energy difference between ramsdellite and pyrolusite.

First Principles calculations show that ramsdellite is stabilized by the addition of Ruetschi defects. To study the effect of these defects on the structural stability of γ-MnO_2, Monte Carlo simulations in the presence of Ruetschi defects were performed.

3.5.2 Monte Carlo with Mn-deficient MnO_2

A qualitative model was devised to simulate the effect of Ruetschi defects on the structural stability. In this model, the Mn atoms were replaced at random by Ruetschi defects, which were assumed to be immobile. The model assumes Ruetschi defects to interact just like the Mn they replace except that the in-plane nearest neighbor Mn atoms around these defects experience a reduced electrostatic repulsion (reduced by *S*). This can be rationalized by considering that Ruetschi defects replace a single Mn^{4+} ion with 4 H^+ ions. The H ions form a more distortable, less concentrated charge distribution that is less

ionic than the Mn and hence Ruetschi defect provides less electrostatic repulsion than a Mn ion. The value of S can be calculated by fitting the interactions to the First Principles energies of pyrolusite and ramsdellite with Ruetschi defects. Pyrolusite has 2 in-plane nearest-neighbor Mn atoms around a Ruetschi defect while ramsdellite has 4 in-plane nearest-neighbor Mn atoms around a Ruetschi defect. Therefore, per defect, ramsdellite would be stabilized by energy of $2S$. First Principles calculations show that ramsdellite is stabilized over pyrolusite by about 300 meV per defect. Hence, for our model, we obtained 150 meV as the value of the S parameter.

This in plane nearest neighbor shift (S) can be added to the original cluster expansion as a modification of V_2, allowing us to calculate accurate Mn-vacancy thermodynamics near Ruetschi defects by qualitatively including the effect of Ruetschi defects.

Results

The results of the Monte Carlo simulations incorporating Ruetschi defects are shown in Figure 3.22. This figure is a snapshot of the system with 5% Ruetschi defects at room temperature, after equilibration for 3000 Monte Carlo steps. When there are no Ruetschi defects in the system, pyrolusite is the ground state and there are no excitations at room temperature. Clearly, the Ruetschi defects introduce a high level of disorder in the structure. Both ramsdellite units and twins can be observed in Figure 3.22. This is in agreement with First Principles calculations, which show that ramsdellite is stabilized on addition of Ruetschi defects. The stabilization of ramsdellite over pyrolusite is also evident in the variation of the 2NN correlation with defect concentration (Figure 3.23).

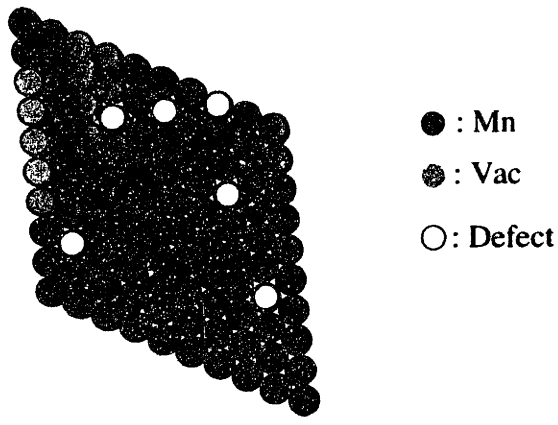

Figure 3.22: Snapshot of the Mn-vacancy lattice including 5% Ruetschi defects at room temperature. Figure shows a basal plane of the hexagonal lattice. Dark and light circles represent Mn and vacancies respectively. Empty circles represent Ruetschi defects.

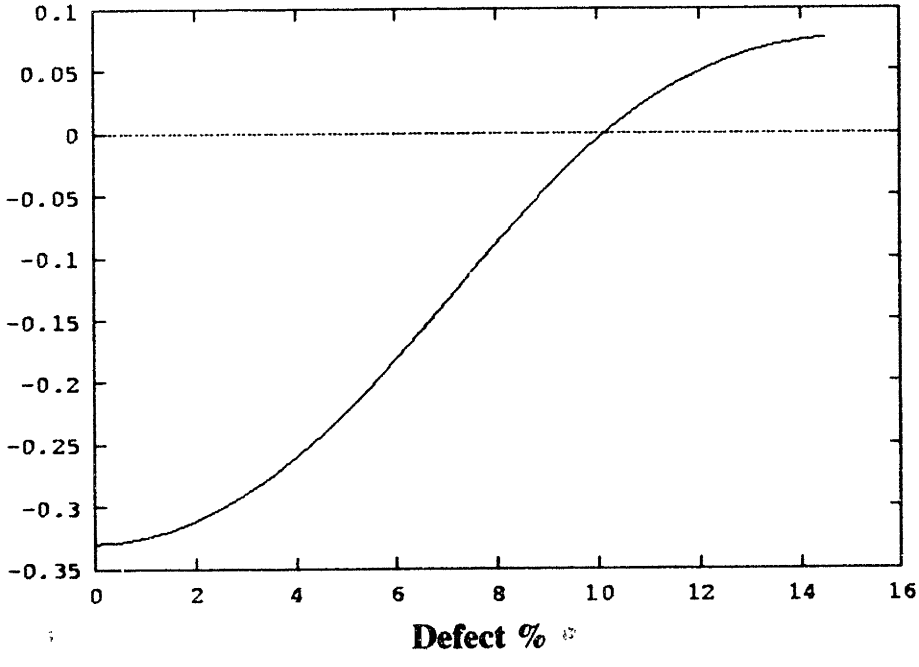

Figure 3.23: Variation of the 2NN correlation with defect concentration for MnO_2. Figure obtained from Monte Carlo simulations equilibrated at T=300K.

When there are no defects, the 2NN correlation has a value of –0.33, which exactly corresponds to that of pure pyrolusite. However on addition of Ruetschi defects, the 2NN correlation starts varying and on addition of 10% defects, the correlation becomes greater than zero, which corresponds to a composition that has 50% ramsdellite and 50% pyrolusite based on just the 2NN correlation.

Thus, Ruetschi defects stabilize ramsdellite over pyrolusite because ramsdellite has more Mn neighbors near a defect as compared to pyrolusite. The Ruetschi defect provides less electrostatic repulsion than a Mn ion and hence Mn ions are more stable near a Ruetschi defect than near another Mn ion. Since ramsdellite has more Mn neighbors near a defect as compared to pyrolusite, it is relatively stabilized by Ruetschi defects.

3.6 Summary

Both synthetic and natural MnO_2 appear in a large number of polymorphs. Our First Principles calculations confirm that even though the effective Mn-Mn interactions are very large and repulsive, a large number of structures are nearly degenerate in energy with pyrolusite. These structures can often be seen as different compromises to the frustration of the V_1-V_2-V_3 triangle of repulsive interactions. While pyrolusite prefers to maximize its in-plane Mn-vacancy NN pairs, ramsdellite sacrifices these to maximize its out-of plane Mn-vacancy pairs. It is worth pointing out that since the in-plane and out-of plane pairs are along different crystallographic axes, small changes in these parameters, as for example may occur with stress or defects, could modify the energy balance between ramsdellite and pyrolusite.

All of the low energy structures have the lines of face sharing octahedra along the c-axis occupied alternately by Mn atoms and vacancies. This can be rationalized by the

short distance between these octahedral sites, which prevents simultaneous occupation of them by Mn. This strong correlation along the c-axis turns the disorder problem into one of organizing long Mn-vacancy-Mn chains. This can be turned into a two-dimensional model by specifying the ion in the chain that penetrates a given plane perpendicular to the chain. The effective interactions between these chains, and per unit length of the chain, are very small, of the order of 20 meV, which may be the cause of the structural diversity of MnO_2.

The First Principles calculations also reconfirm the important role of magnetism in the energetics of manganese oxides [24]. Only when paramagnetic results are extrapolated from a large number of ferromagnetic and antiferromagnetic configurations does pyrolusite appear as the ground state of MnO_2, in agreement with the general interpretation of experimental results. Our results also establish that there is no thermal disorder in stoichiometric MnO_2 as permutations of the vacancy -Mn- vacancy chains are at high-energy cost. Only when the correlation length is reduced can the system disorder. These ideas have been confirmed by direct Monte Carlo simulation on the lattice model derived from the Density Functional Theory calculations.

The effect of Ruetschi defects, Mn vacancies compensated by 4 protons, is striking. Even at low concentration, we predict that random Ruetschi defects turn ramsdellite into the ground state (at least compared to pyrolusite). This may explain the abundance of ramsdellite in electrochemical MnO_2 (EMD), which is known to contain a substantial number of Ruetschi defects [47]. Our result that the energy of ramsdellite is lowered compared to pyrolusite is in agreement with the experimental observation [55] that Ruetschi defects predominantly occur in ramsdellite. The statement that Ruetschi defects are lower in energy in ramsdellite than in pyrolusite is formally equivalent to our finding that they stabilize ramsdellite over pyrolusite. Our results suggest that a possible

way to control the relative amounts of ramsdellite and pyrolusite in γ-MnO_2 is to control the defect content. We believe that Ruetschi defects prefer ramsdellite as the defects are coordinated by more Mn in ramsdellite than in pyrolusite. The higher Mn coordination of the defect may help to screen its effective negative charge left by the imperfect screening of the 4 protons, which are involved in covalent binding with the surrounding oxygen ions.

In any γ-MnO_2 sample, the concentration of Ruetschi defects may be substantially higher in the ramsdellite units of γ-MnO_2 than the sample average, as the energy for the defect is lowest in ramsdellite and hence Ruetschi defects may segregate there. The transformation of ramsdellite into pyrolusite [56] can now be explained by the loss of water which reduces the Ruetschi defect concentration and hence the stability of ramsdellite.

Monte Carlo simulations on a system with random Ruetschi defects resulted in a structure with well defined ramsdellite structural units and considerable twinning, in apparent agreement with the two-parameter disorder model of Chabre and Pannetier [38]. Ruetschi defects seem to form the nucleus for twins. This can be easily understood by considering that some of the sites in the twin plane have higher coordination by Mn than in the perfect structures (Figure 3.5). Even experimental evidence indicates that Ruetschi defects increase the percentage of twinning in the sample, as can be seen from Table 3.6 [38]. This table compares the percentage of twinning with the amount of Mn vacancies and Mn^{3+} ions for some well-known samples. It clearly shows that as the amount of Ruetschi defects increase, the percentage of twinning increases in the sample.

Sample	O/Mn	x	y	Tw (%)
CMD IBA-11	1.97	0.012	0.059	20
CMD IBA-12	1.94	0.026	0.117	≈10
CMD Sedema WSA	1.97	0.044	0.057	36
EMD Knapsack	1.98	0.080	0.037	> 90
EMD Tekkosha GH	1.97	0.083	0.055	> 90
FEMD (Ruetschi)	1.96	0.087	0.073	> 90

Table 3.5: Comparison of percentage twinning with concentration of Ruetschi defects, for various experimental MnO_2 samples [38]. x indicates % Mn vacancies while y indicates % Mn^{3+} ions in the sample.

We do not yet understand how the disorder-inducing effect of Ruetschi defects can be reconciled with the recent multi-phase model proposed by Heuer [39], though it is possible that Ruetschi defects, if mobile, would organize into more perfect structures.

Chapter 4

Electrochemical properties of γ-MnO_2

4.1 Background

The electrochemical properties of γ-MnO_2 electrodes in alkaline aqueous electrolytes are determined by the thermodynamics and kinetics of proton and electron insertion into the MnO_2 host structure. The cathode half-cell reaction can be formally written as:

$$MnO_2 + xH^+ + xe^- \rightarrow MnOOH_x \quad (4.1)$$

Remarkably, considerable discussion still exists on the location of protons and their bonding type in MnO_2 as a function of insertion level. Below, we give a brief description of some of the various models that have been proposed for proton location in γ-MnO_2.

Fitzpatrick et al. [57] performed a Fourier Transform Infrared Spectroscopy (FTIR) study on two samples of EMD (R2 and IBA 19) and studied the vibration spectra at different insertion levels of H. The vibration spectra of EMD contained peaks due to [MnO_6] vibration and O-H vibration (corresponding to protons present near Mn vacancies). On insertion of protons in the EMD samples, for the peaks corresponding to O-H vibration, no change was observed in the area under the peaks until an insertion level, expressed by x in MnO_nH_x, of x=0.63 (R2) and x=0.55 (IBA 19). However, beyond these insertion levels, the area under the peaks showed a continuous change. Since H insertion up to x=0.63 (R2) and x=0.55 (IBA 19) caused little change in the FTIR patterns, the authors concluded that O-H bonds are not formed by the inserted H and that

the inserted H are mobile in the structure, until x=0.63 (R2) and x=0.55 (IBA 19). Only beyond these levels, H localization occurs with accompanying O-H bond formation, which leads to the observed increase in the area under the peaks.

Fillaux et al. [58] used Inelastic Neutron Scattering (INS) to study the proton locations in manganite (γ-MnOOH), the end product of pyrolusite reduction [38]. Crystallographic data [59, 60], suggests that in manganite, the protons are covalently bonded to the oxygen atoms. Fillaux et al. hence expected certain peaks in the INS spectra of manganite to correspond to O-H vibration, however no such peak was observed. Instead, it was found that the INS spectrum of manganite shows a striking similarity with those of intermetallic hydrides. In hydride systems, protons occupy octahedral or tetrahedral sites in the metal lattice. Hence, Fillaux et al. speculated that H is not associated with any particular oxygen atom in manganite, and that it vibrates around the center of the oxygen octahedron. Based on this premise, the calculated manganite INS spectra was found to closely match those observed from experiments. It was also observed that the INS spectra of reduced EMD (γ-MnO_2) and natural manganite are quite similar and hence, the INS spectra of reduced EMD was interpreted based on the assignment scheme proposed for manganite. Fillaux et al. finally concluded that both, protons in manganite and protons inserted by reduction into γ-MnO_2, are not covalently bound to the oxygen atoms. The protons are more likely to be found at highly symmetrical positions like the center of the oxygen octahedra.

However, the validity of these results has been questioned by authors of various subsequent articles. Chabre et al. [38] claim that the INS spectra results of Fillaux et al. pertain to surface protons, which have a different arrangement than the bulk protons. Kohler et al. [61] performed FTIR spectroscopy on the MnOOH polymorphs and claimed that the findings of Fillaux et al. are in strong disagreement with their refinements. They

also argued that symmetrical H bonds, as proposed by Fillaux et al., are only observed at O-H...O distances below 2.5 Å while in MnO_2, the O-H...O distance is ~ 2.6 Å.

Chabre and Pannetier [38], in their detailed review of the MnO_2-H system had several points to make regarding proton location in MnO_2 system. They claimed that intercalated protons are always covalently bound to the oxygen atoms in both ramsdellite and pyrolusite. They also stated that while pyrolusite contains only one type of oxygen atom, ramsdellite contains two chemically different oxygen atoms (O_{pyr} and O_{planar}) according to their coordination to Mn^{4+}. Since the two oxygens are at different lattice potentials (O_{pyr} is less stabilized by the lattice potential), O_{pyr} is more likely to be hydroxylated than O_{planar}.

Proton intercalation

It is now commonly recognized that γ-MnO_2 electrodes behave as intercalation electrodes in alkaline electrolytes. The discharge of the electrochemical cell occurs through proton and electron insertion into the MnO_2 host structure. γ-MnO_2 is not a homogeneous phase since the presence of structural defects implies the existence of several non-equivalent Mn sites in the lattice. Nevertheless, it is still frequently accepted that the proton insertion process occurs homogeneously and that a single phase is obtained as final product after insertion of one electron per Mn. Various studies have attempted to describe the reduction process in MnO_2 and we below give a brief description of some of them.

Brouillet et al. [62] using a thin-film electrode and working under galvanostatic and potentiostatic conditions showed that the kinetics of the MnO_2 reduction can be described by assuming proton diffusion in MnO_2. It was then assumed that reduction of EMD leads to the formation of groutite. The reduction process was considered as

homogeneous since the potential was observed to decrease continuously with the degree of reduction up to one e^- per Mn and the lattice parameters were observed to expand continuously in the early stage of reduction.

Bell and Huber [63] noticed that the slope of the open circuit voltage (OCV) curves for the reduction process exhibits an abrupt change at about mid-reduction, and hence concluded that reduction of γ-MnO_2 cannot be described by a single Nernst equation up to one e^-/Mn.

Based on XRD studies and OCV measurements, Maskell et al. [64] proposed a two-step process for electrochemical reduction of γ-MnO_2 up to one e^-/Mn. The reduction proceeds, first from MnO_2 to $MnOOH_{0.5}$ and then to MnOOH. This was explained by noting that a Jahn-Teller distortion due to Mn^{3+} occurs at mid-reduction and this leads to different locations of the protons in the 2×1 tunnels of the ramsdellite units of γ-MnO_2 before and after mid-reduction.

Kozawa and Yeager [65] observed that after formation of groutite (α-MnOOH), further reduction to Mn^{2+} occurs, which corresponds to a two-phase equilibrium with a voltage plateau. The mechanism of this step involves the dissolution of Mn^{3+} and Mn^{2+} and precipitation of Mn^{2+} as pyrochroite ($Mn(OH)_2$).

Chabre and Pannetier [38] used step potential electrochemical spectroscopy to study the reduction process of various γ-MnO_2 samples. They first showed that no simple physical model could be put forward to describe the reduction of γ-MnO_2 over the full range to one e^-/Mn and then proposed a heuristic description of the reduction process. According to their description, the reduction of γ-MnO_2 ideally proceeds in three definite steps. The initial fast reduction process involves surface protons, which account for 5% of the total manganese content. This is followed by the reduction of Mn^{4+} cations located in the ramsdellite units and concomitant proton intercalation into the tunnels of these

units. This step occurs in two stages separated by a Jahn-Teller distortion induced structural change, which distorts the shape of the tunnels. This is finally followed by a slow step involving the reduction of Mn^{4+} ions located in the pyrolusite units. Chabre and Pannetier also pointed out that the reduction of γ-MnO_2 follows different paths depending on how far from equilibrium it is carried out. Under conditions near thermodynamic equilibrium, an intermediate phase $MnOOH_{0.5}$ analogous to the mineral groutellite is formed. However, if the sample is maintained far from equilibrium, the intermediate phase is either not formed or is a highly disordered structure.

In this present work, we demonstrate the use of computational methods to investigate the location and potential of H in MnO_2. Section 4.2 deals with the location of protons in various MnO_2 and MnOOH polymorphs. In section 4.3, diffusion paths for proton migration are determined for various MnO_2 and MnOOH polymorphs. In section 4.4, features of the experimental intercalation curve are compared with the calculated intercalation curve for ramsdellite. Section 4.5 deals with Ruetschi defects and their effect on the voltage curve. In section 4.6, we discuss the relative stability of groutellite ($MnOOH_{0.5}$) phase and in section 4.7, we summarize our results.

4.2 Proton Location

As mentioned earlier, considerable discussion exists on the location of the protons at the beginning of discharge (low concentrations). In order to correctly identify the location of isolated protons in ramsdellite and pyrolusite, First Principles calculations have been performed. Calculations have also been performed to determine the location of protons in groutite and manganite. In the following section, we discuss the results of these First Principles calculations.

4.2.1 Ramsdellite

There are two symmetry inequivalent types of oxygen atoms (pyramidal and planar) in the ramsdellite structure, distinguished by the bonding angles they make with their Mn neighbors (see Table 4.1). Calculations were performed by placing protons at various locations in ramsdellite and allowing the structure to completely relax. Our calculations indicate that the lowest energy for a proton is near a pyramidal oxygen atom. The proton sits about 1 Å from this oxygen atom and is covalently bonded to it (see Figure 4.1 point A). The proton also forms a weak hydrogen bond with a pyramidal oxygen atom across the 2×1 tunnel, with an O-H distance of ~2.2 Å. Near a planar oxygen atom, the proton is locally stable (see Figure 4.1 point B) but has energy 140 meV higher than that of a proton bonded to a pyramidal oxygen atom. In the tetrahedral and octahedral sites, the proton is not at all stable and it relaxes to the nearest pyramidal oxygen atom (Tetrahedral and octahedral sites are shown in Figure 4.1 points C and D respectively).

In ramsdellite, there is a slight relaxation of the oxygen atoms on proton insertion. When the H atom is placed between two pyramidal oxygen (O) atoms, the O-O distance shrinks from 3.08 Å to 2.98 Å due to weak hydrogen bonding.

4.2.2 Pyrolusite

Pyrolusite has only one type of oxygen atom, in contrast with ramsdellite (see Table 4.1). The intercalated proton forms a covalent bond with an oxygen atom with an O-H distance of ~1.06 Å. It also forms a hydrogen bond with the oxygen atom across the 1x1 tunnel with an O-H distance of ~1.53 Å (see Figure 4.2). The proton easily hops across the tunnel between the two oxygen atoms, with an activation barrier of ≈ 25 meV.

Structure	Experiment	GGA (Antiferromagnetic)
Pyrolusite(β-MnO_2)		
a,b,c (Å)	4.404, 4.404, 2.876	4.444, 4.444, 2.891
Vol (Å^3), β (deg)	55.781, 90	57.10, 90
D(Mn-O1) (Å)	1.884(4), 1.897(2)	1.887-99(4), 1.920(2)
Ramsdellite(R-MnO_2)		
a,b,c (Å)	9.3231, 4.4531, 2.848	9.426, 4.557, 2.895
Vol (Å^3), β (deg)	118.3, 90	124.36, 90
D(Mn-O1) (Å)	1.815(1), 1.896(2)	1.921-3(2), 1.930(1)
D(Mn-O2) (Å)	1.943(2), 1.973(1)	1.905-8(1), 1.911(2)
Manganite(γ-MnOOH)		
a,b,c (Å)	5.304, 5.277, 5.304	5.317, 5.344, 5.283
Vol (Å^3), β (deg)	135.2, 114.38	137.17, 113.96
D(Mn-O1) (Å)	1.977(1), 1.982(1), 2.337(1)	1.966(1), 1.970(1), 2.367(1)
D(Mn-O2) (Å)	1.881(1), 1.893(1), 2.213(1)	1.915(1), 1.932(1), 2.275(1)
D(H-O1) (Å)	0.98	1.104
D(H-O2) (Å)	1.615	1.367
Groutite(α-MnOOH)		
a,b,c (Å)	10.667,2.871,4.554	10.794, 2.898, 4.552
Vol (Å^3), β (deg)	139.47, 90	142.28, 90
D(Mn-O1) (Å)	1.895(2), 2.174(1)	1.920-7(2), 2.242(1)
D(Mn-O2) (Å)	1.965(2), 2.338(1)	1.963-6(2), 2.361(1)
D(H-O1) (Å)	1.818	1.435
D(H-O2) (Å)	0.807	1.082

Table 4.1: Comparison of experimental and calculated structural parameters for various MnO_2 and MnOOH polymorphs.

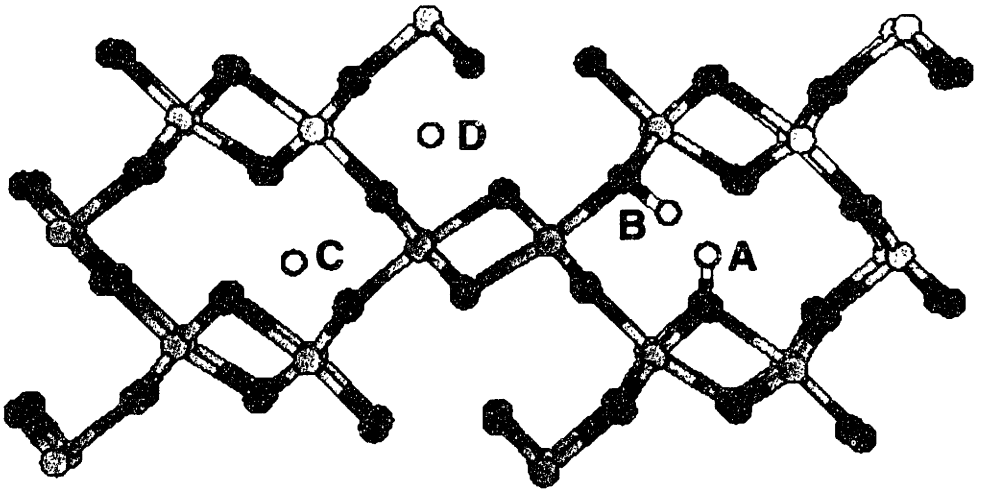

Figure 4.1: Plausible locations of protons in ramsdellite. A represents proton site close to a pyramidal oxygen atom; B represents proton site close to a planar oxygen atom; C represents a tetrahedral site and D represents an octahedral site. Light and dark circles represent Mn and oxygen atoms respectively.

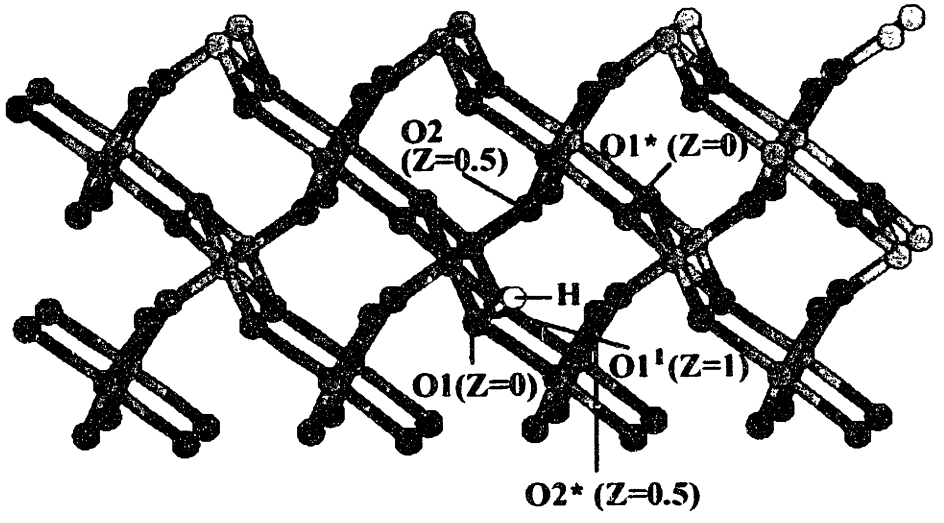

Figure 4.2: Illustration of proton location and plausible proton diffusion paths in pyrolusite. Coordinate z is along the b axis, into the 1×1 tunnel. The symbol ^{1} is attached to an oxygen atom to represent a periodic image of the oxygen atom along the b-axis. The symbol * is attached to an oxygen atom to represent an oxygen atom across the 1×1 tunnel.

This implies that, although the octahedral site at the center of the 1x1 tunnel is not stable, the thermal motion is such that the average proton position will appear to be at an octahedral center (this could explain the observations of Fillaux et al [58]).

In pyrolusite, there is a very large relaxation of the structure on proton insertion. When the H atom is put between two oxygen atoms, the O-O distance shrinks from 3.23 Å to 2.59 Å due to hydrogen bonding.

4.2.3 Groutite

Groutite (α-MnOOH) is the protonated form of the ramsdellite structure. It has a distorted structure compared to ramsdellite, primarily due to the Jahn-Teller effect and hydrogen bonding [61]. In order to verify the location of protons in groutite, calculations were performed by starting with experimental positions and allowing the structure to completely relax. The calculated structural parameters of groutite, obtained on relaxation, are shown in Table 4.1. From the table, one can observe that the Mn-O distances are considerably different in groutite compared to ramsdellite, which is due to the Jahn Teller distortions. The structure of groutite is shown in Figure 4.1. Calculations show that proton in groutite forms a covalent bond with a pyramidal oxygen atom and reside at a distance of 1.08 Å from the pyramidal oxygen atom. It can also be seen that the proton forms a hydrogen bond with the planar oxygen atom across the 2×1 tunnel, with an O...H distance of 1.435 Å. In ramsdellite, protons are not hydrogen bonded to the planar oxygen atom across the tunnel and hence, protons have different configurations in groutite and ramsdellite.

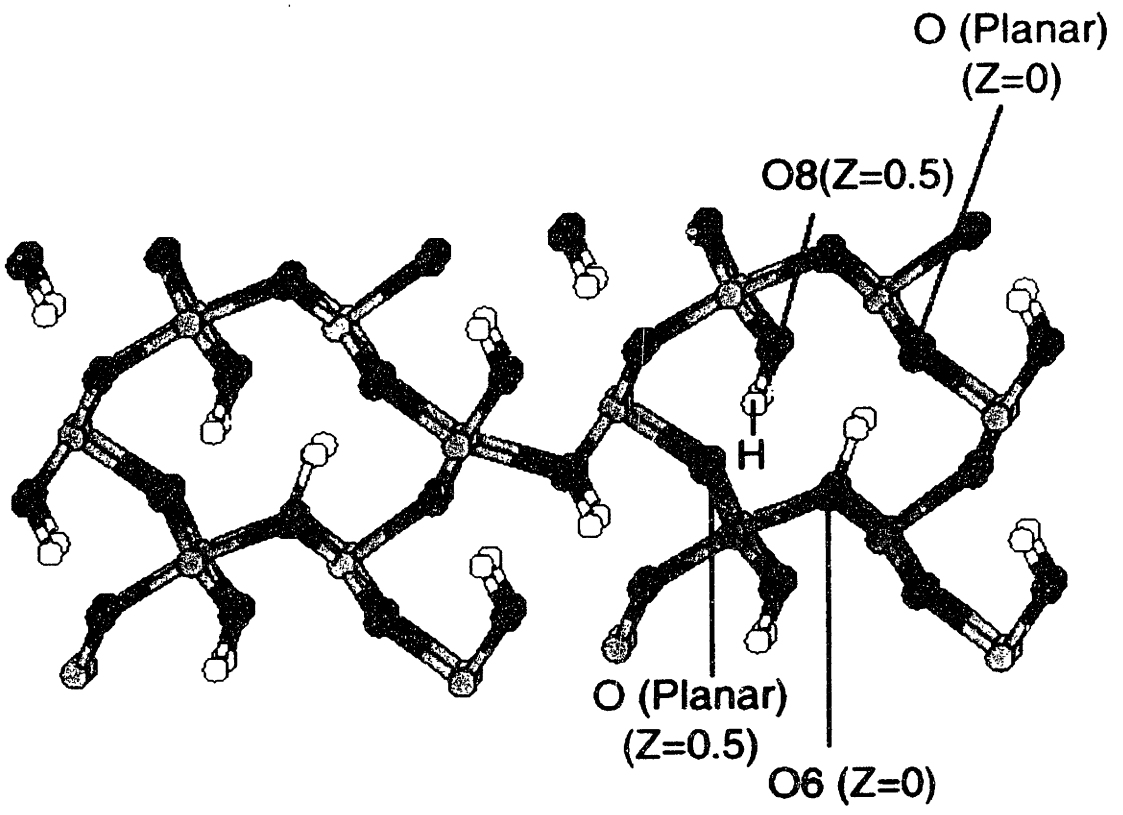

Figure 4.3: Illustration of proton location and plausible proton diffusion paths in groutite. The MnO_2 lattice is distorted in groutite due to Jahn-Teller distortion and hydrogen bonding. O6 and O8 represent pyramidal oxygen atoms while O(planar) represent planar oxygen atoms. Coordinate z is along the b axis, into the 2×1 tunnel.

4.2.4 Manganite

Manganite (γ-MnOOH) is the protonated equivalent of the pyrolusite structure. Manganite also has a distorted structure due to Jahn Teller distortions and hydrogen bonding [61]. Structural calculations for manganite were performed by starting with experimental parameters and allowing the structure to completely relax. The calculated structural parameters for manganite are shown in Table 4.1. Similar to the case in groutite, there is a significant difference between the Mn-O distances in manganite and pyrolusite, thus pointing to the effect of Jahn Teller distortions. The calculations in manganite indicate that protons are covalent bonded to an oxygen atom and hydrogen

bonded to the oxygen atom across the tunnel (see Figure 4.4). However, in manganite, the calculated O-H...O distance is only ≈ 2.47 Å. Hence, the bond length of the O-H covalent bond (1.104 Å) is not that different from the O...H hydrogen bond length (1.367 Å). Furthermore, the activation barrier for a proton jump between these two oxygen atoms is very low (< 25 meV). This suggests that the protons in manganite vibrate around the octahedral sites, which explains the observations of Fillaux et al. [58].

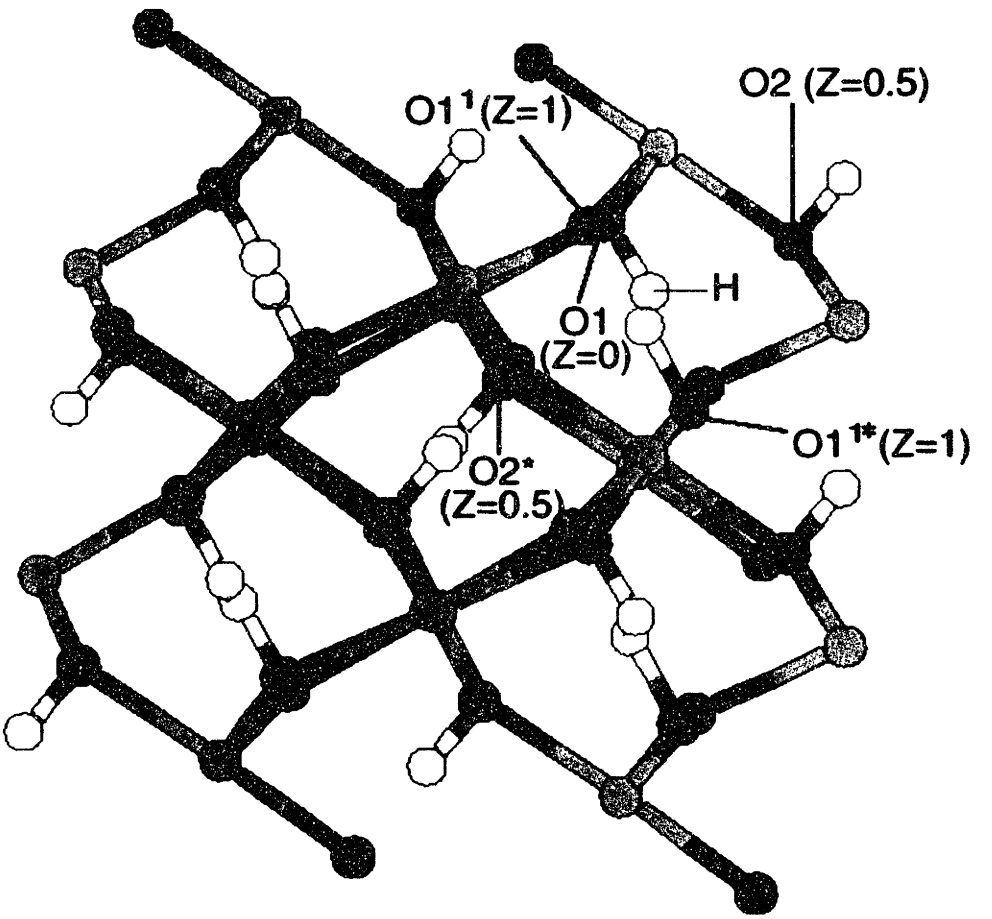

Figure 4.4: Illustration of proton location and plausible proton diffusion paths in manganite. The MnO_2 lattice is distorted in manganite due to Jahn-Teller distortion and hydrogen bonding. Coordinate z is along the b axis, into the 1×1 tunnel. The symbol ¹ is attached to an oxygen atom to represent a periodic image of the oxygen atom along the b-axis. The symbol * is attached to an oxygen atom to represent an oxygen atom across the 1×1 tunnel.

4.3 Proton Diffusion

Diffusion values for protons in EMD found in the literature can range from 10^{-11} to 10^{-16} cm^2/s, although recent assessment of this data by Chabre and Pannetier [38] suggests that the range is 10^{-14} to 10^{-16} cm^2/s. This rather slow diffusivity seems to conflict with the idea of delocalized protons [57]. Therefore, Molecular Dynamics simulations and First Principles calculations utilizing the elastic-band method were performed to accurately determine the activation barriers for proton diffusion.

4.3.1 Molecular Dynamics

In order to better understand the mechanisms of proton diffusion in ramsdellite, Molecular Dynamics (MD) simulations involving protons in a ramsdellite lattice were initially performed.

The MD simulation on ramsdellite gave the following picture for diffusion. The proton is found to move almost exclusively between pyramidal oxygen atoms, which forces the diffusion to take place along the center of the 2×1 channels. Diffusion occurs by what we call a rotation and jump mechanism. For a given oxygen pair, the proton jumps between the oxygen along the line joining them. In order to move between a different oxygen pair, the proton rotates part way around a given oxygen until it is along the line between the new oxygen pair. A schematic illustration of this hopping method is shown in Figure 4.5. It is expected that protons easily rotate around the oxygen atom, while jumping between the oxygen involves crossing a significant energy barrier.

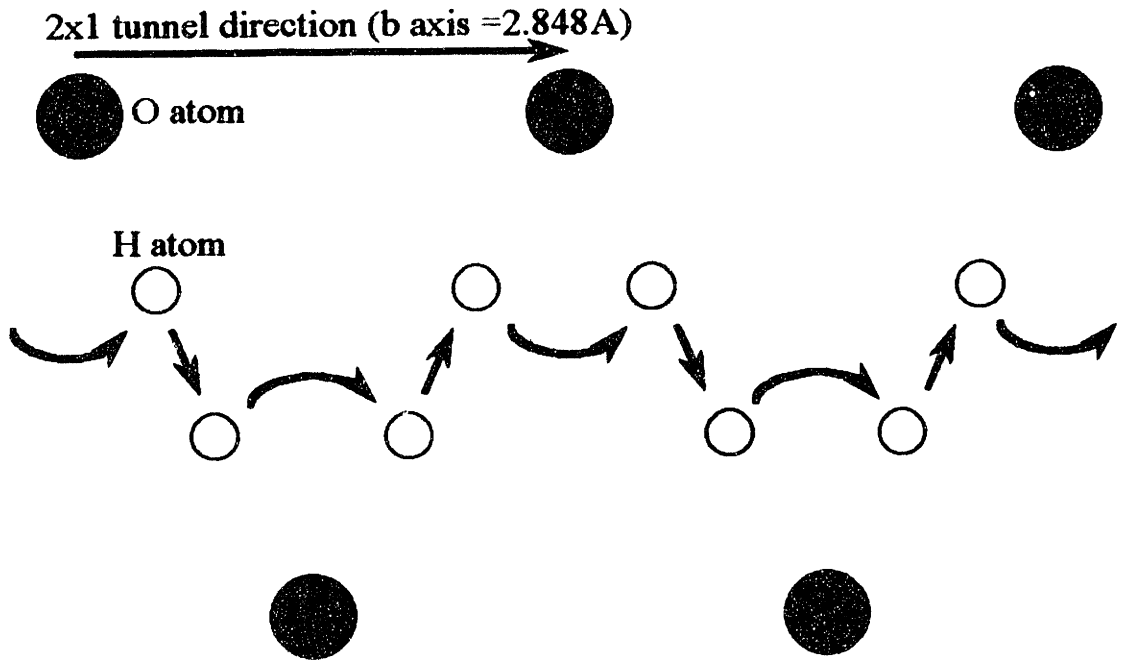

Figure 4.5: Schematic illustration of the proton hopping mechanism in ramsdellite. Dark circles represent pyramidal oxygen atoms aligned along the 2x1 tunnels of ramsdellite. Protons jump and rotate between oxygen atoms and thus diffuse into the tunnel.

4.3.2 Elastic band calculations

Plausible proton diffusion paths were determined in various MnO_2 and MnOOH polymorphs and elastic band calculations were performed to determine the activation energy barrier for each of these diffusion paths. A diffusion path was considered plausible if satisfied the following criteria:

- It involves hops between proton sites close to an oxygen atom (The proton should form a covalent bond with the oxygen atom).
- It links proton sites along the same tunnel. It was found that a proton hop between sites located in different tunnels in ramsdellite involves an activation energy barrier

>>1 eV. Hence, these paths were not considered further for elastic band calculations. It involves no greater than 2 interstitial hops from start to finish.

- It involves movement of the proton along the tunnel. (In pyrolusite, the proton rapidly hops between oxygen atoms located on the same plane perpendicular to the axis of the tunnel (b axis), but this does not constitute diffusion).

Screening the candidate pathways with these criteria was essential to reduce the many probable diffusion paths to a manageable list of candidates meriting further consideration.

Ramsdellite

The plausible diffusion paths in ramsdellite were determined based on the criteria mentioned above and elastic band calculations were performed along these paths. Since periodic cells were used in the calculations, calculations were essentially performed for $MnOOH_{0.25}$. In order to simulate the diffusion of isolated protons more accurately, the calculations are done with cell parameters fixed to those of the ramsdellite structure (see Table 4.1). However, all internal degrees of freedom were fully relaxed for each periodic image.

Calculations on these diffusion paths indicate that diffusion along the center of the 2×1 tunnel is the most stable path. This is in accordance with the results obtained from the Molecular Dynamics simulation. The activation energy for this path (O6 → O8) has been determined to be 200 meV. Refer to Figure 4.6 for all atom labels. Coordinate z in the figure is along the b axis, into the tunnel.

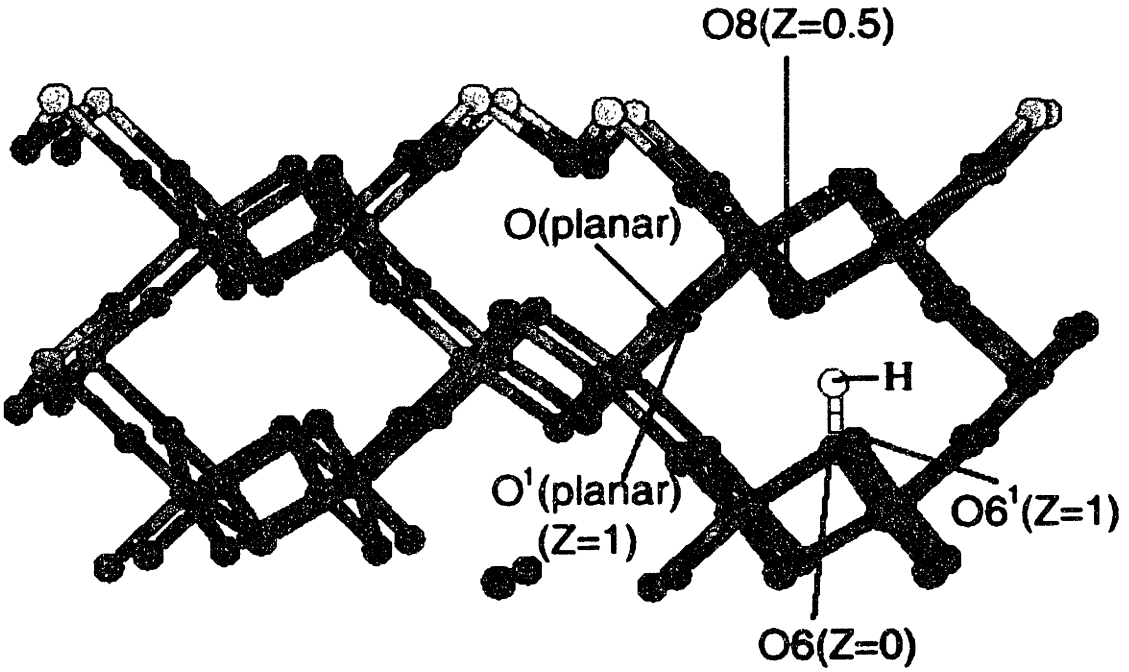

Figure 4.6: Illustration of the possible diffusion paths in ramsdellite. O6 and O8 represent pyramidal oxygen atoms while O(planar) represent planar oxygen atoms. Coordinate z is along the b axis, into the 2x1 tunnel. The symbol ^{1} is attached to an oxygen atom to represent a periodic image of the oxygen atom along the b-axis.

The results for the other possible paths are as follows:

The direct diffusion path O6(pyr) → $O6^{1}$(pyr) is unstable as H hops to an O8 position before hopping to a $O6^{1}$ position.

The diffusion path O(planar) → O^{1}(planar) has an energy barrier greater than 1 eV.

The diffusion path O8(pyr) → O(planar) also has an energy barrier greater than 1 eV.

As mentioned earlier, hopping from one tunnel to another has a very high-energy barrier (>>1 eV).

Therefore, *ab initio* calculations confirm the results of MD simulations and we believe that protons in ramsdellite move almost exclusively between pyramidal oxygen atoms in the same tunnel, according to the mechanism shown in Figure 4.5.

Pyrolusite

To calculate activation energy barrier for proton diffusion in pyrolusite, elastic band calculations analogous to those used in ramsdellite were employed. Here, calculations were again performed in $MnOOH_{0.25}$ with fixed pyrolusite (MnO_2) cell parameters. All internal degrees of freedom were fully relaxed for each periodic image.

Based on elastic-band calculations, the most stable diffusion path for proton diffusion in pyrolusite is O1 → O2 (or O2*) (see Figure 4.0). The activation energy barrier for this path was determined to be 575 meV.

The results for the other possible diffusion paths in pyrolusite are as follows:

The direct diffusion path O1 → $O1^1$ was presumed to be unstable because the proton must hop to either O2 (or O2*) before hopping to an $O1^1$ position.

The barrier for an O1 → $O1^*$ hop is ≈ 25 meV. However, this does not constitute diffusion, as both the oxygen atoms are in the same plane along the tunnel and the proton merely keeps hopping between these two oxygen atoms. This hop is a low-energy hop because the introduction of protons causes the lattice to relax dramatically and the two oxygen atoms are brought very close to each other due to hydrogen bonding.

The activation barrier is much higher in pyrolusite than in ramsdellite. Hence, De-Wolff defects [41] (i.e. pyrolusite units) will very likely reduce the electrochemical reactivity of γ-MnO_2 by hindering proton diffusion.

α-PbO_2

The effect of twinning on the diffusion process was evaluated by studying H migration in the α-PbO_2 structure, the 100 % twinned equivalent of the pyrolusite structure [38]. Like pyrolusite, this structure has only one type of oxygen atom. Calculations on this structure indicated that the intercalated proton is covalent bonded to an oxygen atom with an O-H distance of ~1.12 Å.

Elastic-band calculations indicate that the lowest energy barrier diffusion path in this structure is a two-step process. H initially hops from an O3 position to an O6 position and the barrier is small for this jump (see Figure 4.7). It then rotates and jumps to an O4 position. The activation barrier is ~1.2 eV for this jump. The direct diffusion path (O3 → $O3^1$) is presumed unstable as this distance is ~3.8 Å and H hops to several intermediate O atoms before hopping to $O3^1$ position.

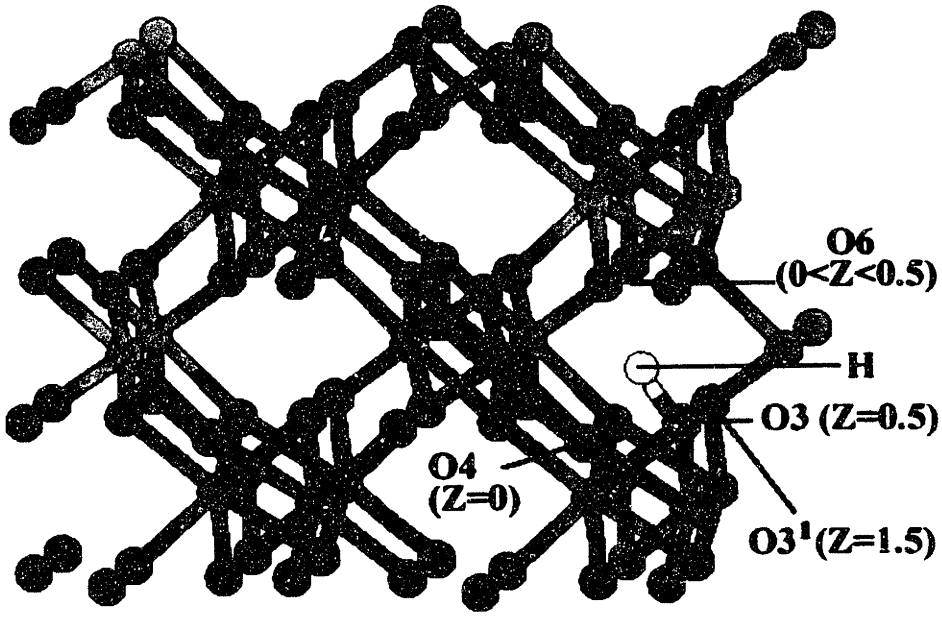

Figure 4.7: Illustration of the possible diffusion paths in twinned pyrolusite (α-PbO_2). Coordinate z is along the b axis, into the tunnel. The symbol ^{1} is attached to an oxygen atom to represent a periodic image of the oxygen atom along the b-axis.

From these calculations, it can be observed that twinning the pyrolusite structure qualitatively changes the diffusion path and increases the activation barrier significantly. These calculations hence suggest that twinning will hinder proton diffusion in MnO_2.

Groutite

Groutite is the protonated form of the ramsdellite structure. In groutite, each of the pyramidal oxygen atoms is involved in a covalent bond with a proton. The proton is also hydrogen bonded to a planar oxygen atom (refer to section 4.2).

Diffusion calculations were performed in this structure by introducing a vacancy near a pyramidal oxygen atom and determining the energy barrier for a proton jump from a nearby filled site to the vacancy. Due to the finite size of the cell, calculations have been performed for $MnOOH_{0.75}$. However, in order to simulate the presence of isolated vacancies more accurately, the calculations are done with cell parameters fixed to those of the MnOOH structure (see Table 4.1), but with full internal relaxation of all periodic images.

Calculations indicate that the diffusion path in this structure is analogous to that in ramsdellite and goes along O6(pyr) → O8(pyr) (see Figure 4.3). The activation barrier for this path is ≈ 400 meV. The path O(pyr) → O(planar) is found to be unstable as the proton is not stable near a planar oxygen atom.

Thus, in groutite, even though the diffusion path is same as in ramsdellite, the activation barrier is significantly higher. We expect this to be primarily due to the Jahn-Teller distortion of the structure. As we will show later, we believe that the presence of other H is likely to have a small effect because of the weak H-H interactions in the system.

Manganite

Manganite (MnOOH) is the protonated equivalent of the pyrolusite structure. As was done with groutite, diffusion calculations were performed in manganite by the introduction of a vacancy. Calculations indicate that the diffusion path is different in manganite as compared to pyrolusite. In manganite, the O1 → $O1^{1*}$ path is the stable lowest-energy diffusion path (see Figure 4.4). The barrier for this path is ≈ 1eV. In pyrolusite, this direct path was found to be unstable since the proton jumps to an intermediate O2 position before hopping to the $O1^{1*}$ position. However, in manganite this is not possible because there is already a proton attached to the O2 atom in the adjacent tunnel. It is not energetically favorable for two protons to be attached to the same oxygen atom and the intermediate O2 position is no longer a low energy metastable state.

In manganite, the activation barrier is considerably higher than in pyrolusite. This is due to the Jahn-Teller distortion and H-O-H interactions. The H-O-H interaction makes the O2 position less stable and hence changes the diffusion path.

4.4 Intercalation Curve

4.4.1 Experimental Intercalation Curve

Various experimental studies have been performed to measure the discharge curve for γ-MnO_2. However, there is a large variation in the intercalation curves published by various authors. This is primarily because the intercalation process in γ-MnO_2 is very dependent on experimental conditions. Electrolyte concentration, rate of reduction, sample preparation and content are all features that significantly alter the intercalation curve. However, the following features are normally associated with differential voltage

curves of conventional EMD samples under normal reduction conditions (potentials are measured vs Hg/HgO) [38]:

- The first peak of the reduction process occurs around +0.1 V. This peak is attributed to the reduction of Mn^{4+} ions located at the γ-MnO_2 surface. Calculations show that for γ-MnO_2 grains with a size of around 1000Å, about 5% of manganese cations lie on the surface layer of the grain.
- The next peak is observed between +50mV and −150 mV. This broad peak is assigned to the reduction of the ramsdellite units by intercalation of protons into the tunnels of its structure. The nature and range of this peak depends a lot on the experimental conditions. When MnO_2 samples are reduced closed to their equilibrium condition, this peak splits into two peaks. The reduction of ramsdellite under equilibrium reduction conditions takes place in two steps. The first step is a homogeneous reduction process, which transforms ramsdellite MnO_2 into $MnOOH_{0.5}$ (groutellite) and retains the shape of the ramsdellite tunnels. This is separated from the next step by a structural phase transformation, which is caused by Jahn-Teller distortion of the [MnO_6] octahedra. The next step, which transforms groutellite (i.e. $MnOOH_{0.5}$) into groutite (α-MnOOH), is characterized by the propagation of the Jahn-Teller distortion through the lattice and the formation of a strong hydrogen bonding network. This two-step equilibrium reduction of ramsdellite is assumed to correspond to the two peaks observed near equilibrium conditions. Under non-equilibrium conditions, the two steps occur simuitaneously and hence, only one peak is observed in the differential voltage curve. This description holds true for dilute electrolytes. In concentrated electrolytes, Mn^{3+} ions dissolve in the electrolyte and cause additional slow transformations.

- A peak is observed between –200 mV and –400 mV, which corresponds to the reduction of the pyrolusite units in MnO_2. Pyrolusite is slowly reduced to manganite (γ-MnOOH).
- Below –430 mV, further reactions take place in concentrated electrolytes, which leads to formation of $Mn(OH)_2$ (pyrochroite).

Since experimental intercalation curves show many features that are still not completely understood, First Principles calculations combined with Monte Carlo simulations were performed in order to study the intercalation process in MnO_2 and to obtain a calculated intercalation curve.

4.4.2 Cluster Expansion

In this work, we decided to calculate the intercalation curve for ramsdellite, using the cluster expansion formalism (refer to section 2.2.2). To determine the H-vacancy lattice, we considered all the plausible sites for proton location in the ramsdellite-groutite system. The various plausible proton locations are tetrahedral sites, octahedral site, sites close to a planar oxygen atom and sites close to a pyramidal oxygen atom. Octahedral and tetrahedral sites, however, have a very high energy for proton location (refer to section 4.2) and the probability of proton residing in these sites is negligible. Hence, these sites are unlikely to contribute to the thermodynamics of proton insertion in the ramsdellite system and are therefore ruled out from the H-vacancy lattice. Similarly, sites close to the planar oxygen atoms have a high energy for proton location and hence they have also been ruled out from the H-vacancy lattice. Consequently, the only plausible proton sites left in the ramsdellite-groutite system are sites close to the pyramidal oxygen atoms. Groutite has two sites for proton location (near the pyramidal oxygen atoms) within the 2×1 tunnels. Hence, in our calculations, we have assumed these sites to be the

H-vacancy lattice in the ramsdellite-groutite system. The various clusters used in the calculation are shown in Figure 4.8. In addition to a constant, a point cluster and 5 pair clusters were used for the fit. The energies of 9 different H-vacancy arrangements, corresponding to different proton intercalation levels in ramsdellite, were calculated and were used to fit the 7 ECI. Least squares procedures [66] were used to optimize the fit and the rms error for the fit was calculated to be 4 meV.

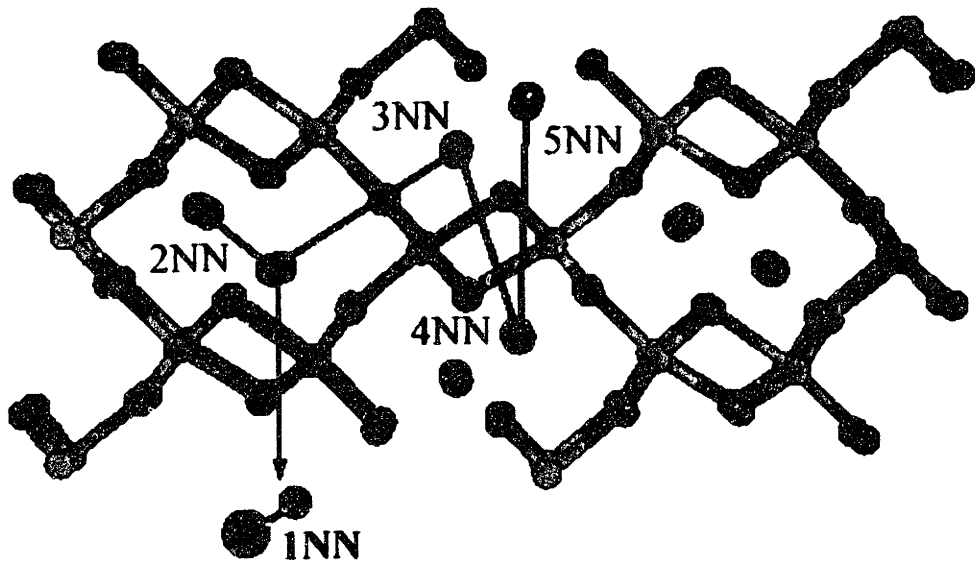

Figure 4.8: The clusters on the H-vacancy sublattice used in the cluster expansion.

The strength of the various interactions obtained from the cluster expansion fit are shown in Table 4.2. From the table, it can be observed that the values of all interactions, in the order of a few meV, are very small. This implies that H-H interactions are weak in this system. In addition, it can also be observed that all interactions are attractive except along the c-axis direction (This is the only interaction where H repel each other). Figure 4.9 shows that the formation energy is positive for all the intermediate compositions

Cluster	Interactions (eV)
Const.	-26.105
Point	2.121
1NN	0.009
2NN	-0.007
3NN	-0.015
4NN	-0.002
5NN	-0.013

Table 4.2: H-vacancy interactions in ramsdellite.

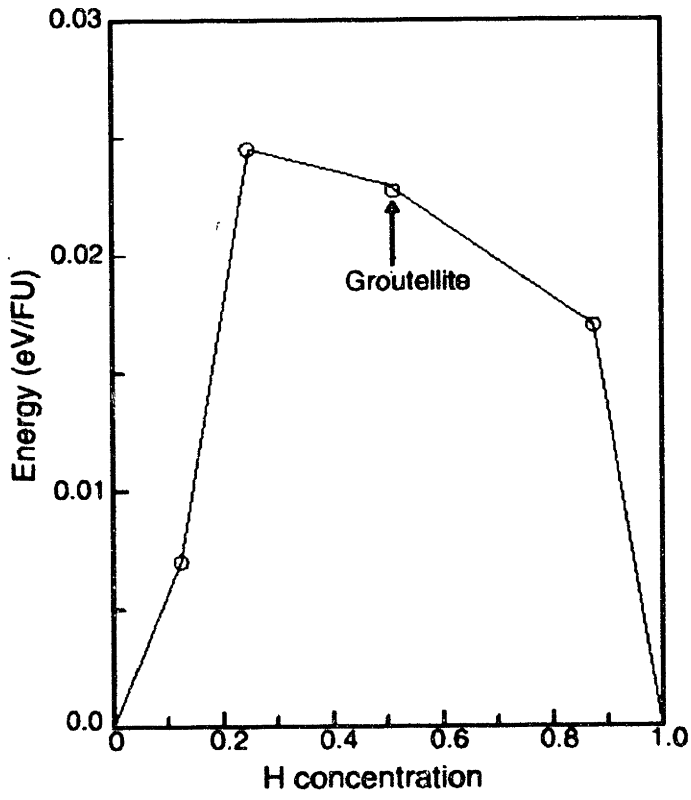

Figure 4.9: Plot of formation energy for the ramsdellite-$MnOOH_x$ system.

between ramsdellite and groutite. This suggests that the system is phase separating, i.e., any intermediate compound is less stable than the equivalent mixture of ramsdellite and groutite. This is very surprising since we expect H to repulse each other (due to electrostatics) and the system to therefore order. This unusual behavior is probably due to the Jahn Teller effect and H-bonding in groutite. In addition, as we will show later, coherency effects can have a significant impact on the ordering behavior of the system.

In order to obtain an intercalation curve, Monte Carlo simulations were performed on the H-Vacancy lattice.

4.4.3 Monte Carlo simulations

The voltage curve is related to the chemical potential of the H within the cathode host (i.e. γ-MnO_2) according to eqn. (2.6). The chemical potential of H within γ-MnO_2 can be obtained using grand canonical Monte Carlo simulations. Simulations were performed at room temperature (300 K) with a 10×10×10 supercell of the primitive orthorhombic cell (4 lattice sites per cell) containing a total of 4000 lattice sites. The number of Monte Carlo steps per site was in the range 2000-2500 for each temperature and of those, the first 1000 were excluded from calculations of thermodynamic quantities to allow for equilibration.

4.4.4 Comparison of Intercalation Curves

In order to study the features of experimental curves, they need to be compared with the calculated intercalation curve. An experimental curve (obtained from Energizer Corporation), the calculated ramsdellite intercalation curve and an ideal curve ($V=kT\ln(x/(1-x))$; assuming only entropic effects in the system) have been plotted in Figure 4.10. Figure 4.10 is a plot of the intercalation voltage versus the proton concentration (x in $MnOOH_x$). It is assumed that the initial features of the experimental

intercalation curve are due to reduction in ramsdellite units and that reduction in pyrolusite occurs only in the later stages of the reduction process. Therefore, the latter part of the experimental curve (corresponding to pyrolusite reduction) has been removed and the experimental curve has been rescaled in figure 4.10, in order to focus on the intercalation of the ramsdellite units. The three curves are plotted in such a manner that the centers of all the three curves coincide. Note that this fixes the absolute voltage for the calculated and ideal intercalation curve.

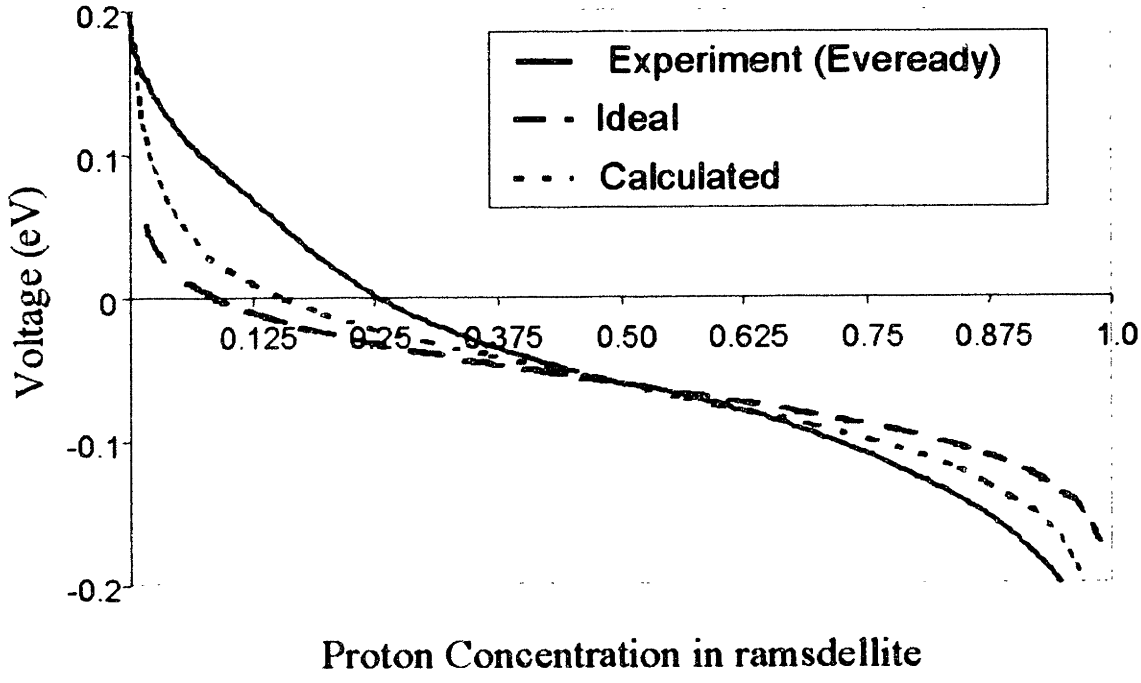

Figure 10: Plot of the experimental, ideal and calculated intercalation curve for ramsdellite. The experimental curve was obtained from Energizer Corporation.

On comparing the different curves, it can be observed that the ideal curve is much too flat. This is to be expected since the ideal curve assumes no interaction between the protons but this is not true in reality. The calculated ramsdellite curve fits reasonably well with the experimental curve beyond mid-reduction, but in the initial stages of the reduction process, the calculated curve deviates considerably from the experimental curve.

The features of an intercalation curve can be better observed by calculating the differential voltage curve. The experimental differential voltage curve (see Figure 4.11) shows a broad peak until x=0.2, which is not observed in our calculations and this is a significant source of the discrepancy between the two curves. The broad experimental peak has normally been attributed to surface protons, which have not been accounted for in our calculations and this could be a possible reason for the discrepancy. However, it must be noted that irrespective of our calculations, there is a problem in assigning the experimental peak (until x=0.2) to surface protons. Surface protons can usually account for only ~5 % of the total level of intercalation level [38] and hence they cannot completely explain the presence of the peak, which is observed until x=0.2.

Another possible explanation for the presence of the experimental peak is the effect of Mn defects. In MnO_2, Mn vacancies are compensated by protons and the proton sites near these defects offer a different local environment for incoming protons. Hence, the change in potential should be different when these sites are filled up and this might account for the difference between the initial region of the experimental curve for γ-MnO_2 and the calculated curve for pure ramsdellite, which does not account for Mn defects.

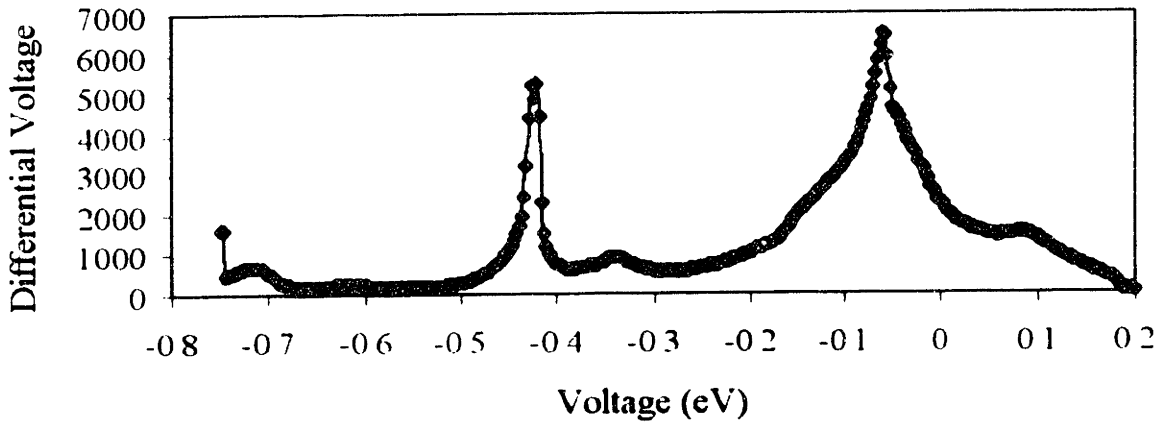

Figure 4.11: Plot of the experimental differential voltage curve. The curve is obtained by differentiating the voltage with respect to the proton concentration. The latter part of the curve (beyond a proton concentration of 0.8) has been removed in order to focus on the intercalation in ramsdellite.

In order to verify this hypothesis, First Principles calculations were performed on ramsdellite with Ruetschi defects.

4.5 Effect of Ruetschi Defects on the Intercalation Curve

A detailed study of the Ruetschi defects can be found in section 3.5. Earlier calculations have shown that ramsdellite is clearly stabilized over pyrolusite by Ruetschi defects. This implies that Ruetschi defects are more likely to be present in the ramsdellite units of γ-MnO_2. To study the effect of Ruetschi defects on the intercalation curve of ramsdellite, First Principles calculations were performed on ramsdellite with Ruetschi defects.

Ruetschi defects replace a single Mn^{4+} ion with 4 H^+ ions. We believe that the H ions form a more distortable, less concentrated charge distribution that is less ionic than the Mn and hence the Ruetschi defect is likely to provide less electrostatic repulsion than

a Mn ion. Due to this reduced repulsion, inserted protons will be more stable near a Ruetschi defect than a Mn ion and hence, according to our claims, the intercalation voltage should be different when Ruetschi defects are present in ramsdellite.

First Principles calculations were performed in ramsdellite to test this hypothesis. Calculations were performed at 12.5 % Ruetschi defect concentration with protons placed at sites adjacent to the Ruetschi defects (as shown in Figure 4.12). The results of these calculations can be observed in Figure 4.13. Figure 4.13 shows the change in voltage on addition of protons in ramsdellite due to the presence of Ruetschi defects. The change in voltage in the absence of Ruetschi defects has been renormalized to zero so that the effect of Ruetschi defects on the intercalation voltage can be visualized properly. As can be observed from the figure, at an intercalated proton concentration of 0.125, the change in voltage is 100 meV more when Ruetschi defects are present in the system.

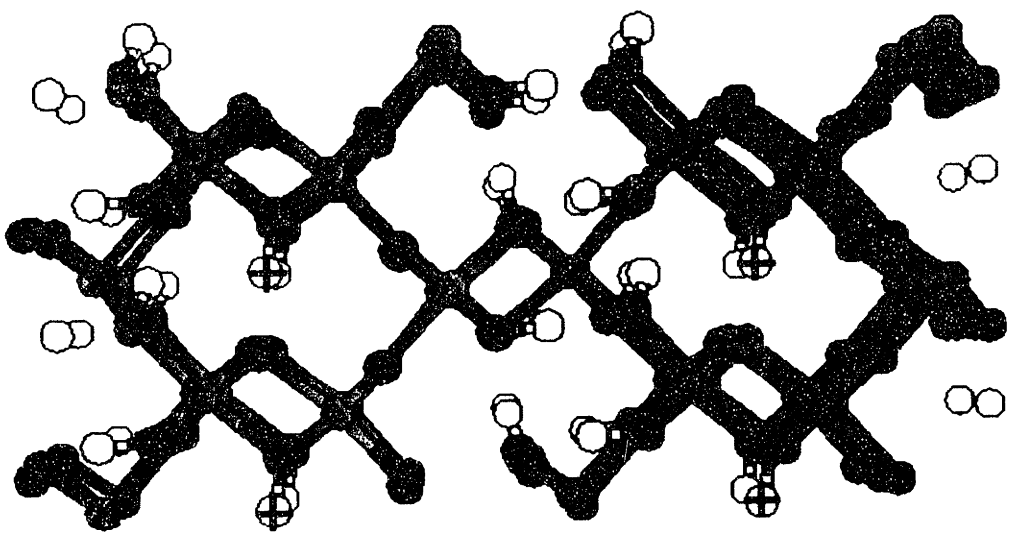

Figure 4.12: Location of intercalated protons in defect ramsdellite. Light and dark circles represent Mn and Oxygen atoms respectively while empty circles indicate protons. × indicates Mn vacancy while + indicates intercalated proton.

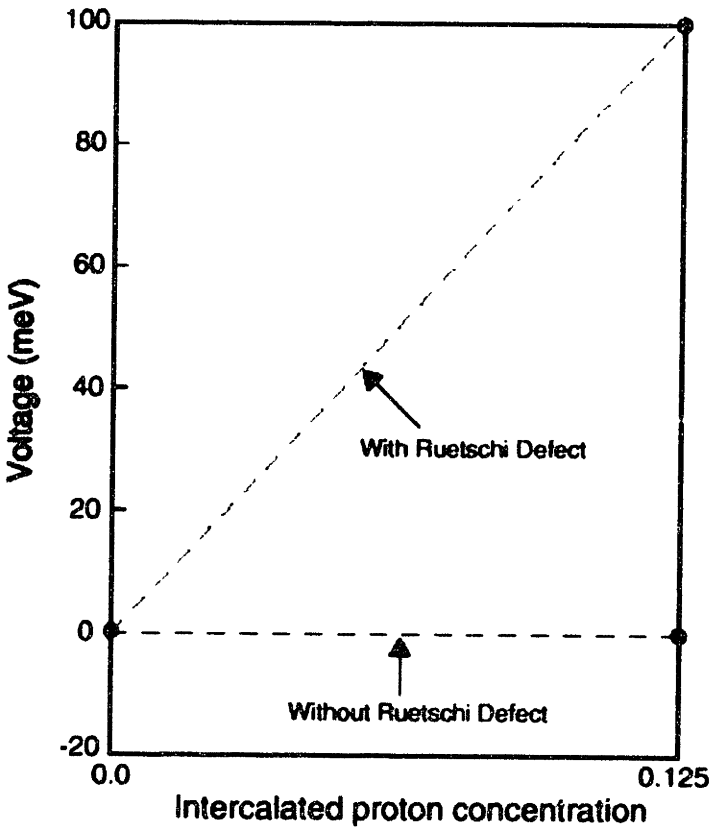

Figure 4.13: Effect of Ruetschi defects on the voltage curve for ramsdellite.

This suggests that protons are more stabilized at sites adjacent to Ruetschi defects, which is in accordance with our reasoning.

Our earlier calculations showed a discrepancy between the experimental intercalation curve and the calculated intercalation curve for pure ramsdellite. At initial proton concentrations, the voltage of the experimental intercalation curve was found to be higher by ≈ 100 meV. The above-mentioned defect calculations would shift the voltage of the calculated intercalation curve upward by a similar magnitude and therefore, Ruetschi defects can explain the discrepancy between the experimental and calculated intercalation curves.

4.6 Understanding Groutellite

There is a significant amount of evidence that under certain circumstances, intercalation of ramsdellite leads to an intermediate $H_{0.5}MnO_2$ (Groutellite) ordered phase. However, this is not seen in our calculations and is somewhat difficult to identify in experiments. A possible explanation could be that groutellite is stable in a coherent system but unstable in the incoherent system. In a coherent system, the lattice parameters have to match across the phase boundaries and this causes strain, whereas in an incoherent system, the lattice parameters are allowed to relax freely and there is no strain across the phase boundaries. First Principles calculations were performed to study the effect of coherency on the stability of groutellite.

Calculations were performed in the ramsdellite-groutite system with the lattice allowed to be incoherent. This implies that all the structures were allowed to relax to their equilibrium lattice parameters. The calculations showed that the formation energy of groutellite is +23 meV per formula unit in an incoherent system (see Figure 4.9). This indicates that groutellite is unstable in an incoherent system. For a coherent system, the lattice parameters across the phase boundary have to match and hence calculations were performed on ramsdellite, groutite and groutellite with lattice parameters fixed to those of groutellite. Under these conditions, the formation energy of groutellite became - 47 meV per formula unit, which indicates stabilization of groutellite. These calculations thus indicate that coherent system leads to the stabilization of groutellite.

To test the hypothesis further, we studied intercalation in a PRPR-intergrowth structure. The PRPR intergrowth has been chosen since it is an idealized representation of the γ-MnO_2 structure, consisting of alternate blocks of pyrolusite and ramsdellite units (as shown in Figure 4.14). In this structure, the ramsdellite blocks are constrained by the surrounding pyrolusite blocks and the lattice is not allowed to relax freely. Hence, the

PRPR system acts like a coherent system for proton intercalation. On intercalation of protons in the ramsdellite blocks, calculations indicated that when the ramsdellite tunnels are half filled (see Figure 4.14), the formation energy for the structure is -17 meV per formula unit. Since a half-filled ramsdellite structure corresponds to groutellite, these calculations indicate that groutellite will be formed during intercalation in a PRPR system.

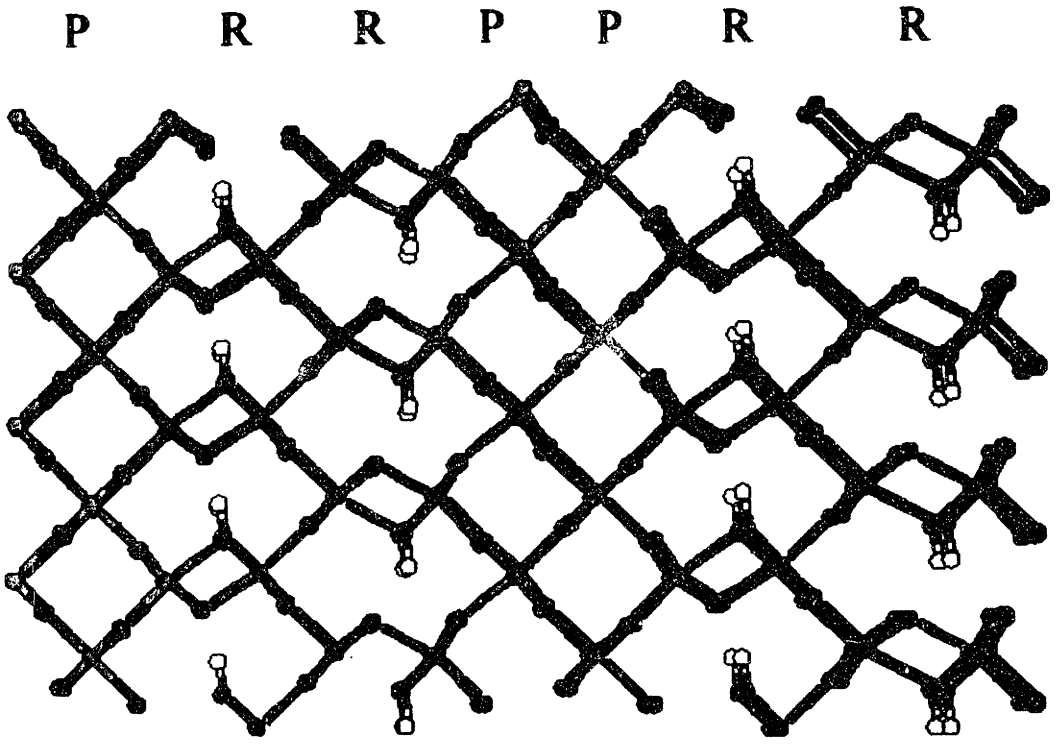

Figure 4.14: Illustration of the PRPR structure. The structure consists of alternate pyrolusite and ramsdellite slabs. Proton intercalation in the ramsdellite slabs is shown in the figure.

It must be noted that the formation energy for groutellite is less negative in the PRPR system compared to the earlier calculations for individual structural units. This is because, in our earlier calculations, energies of ramsdellite and groutite were calculated with groutellite parameters. The strain caused by this constraint on the lattice parameters is much more than the strain caused due to the presence of pyrolusite tunnels in the PRPR system and hence the formation energy is more negative in the earlier calculations. These calculations therefore imply that lattice strain is favorable for groutellite formation.

4.7 Summary

1. Proton location

There has been considerable discussion over the location of protons in MnO_2. Fitzpatrick et al. [57] used FTIR studies on EMD to conclude that protons are delocalized up to a certain discharge level while Fillaux et al. [58] used Inelastic Neutron Scattering (INS) studies to conclude that H vibrates at the center of an oxygen octahedron in γ-MnO_2. Our First Principles results indicate that protons are always covalently bonded to an oxygen atom in various MnO_2 and MnOOH polymorphs. This bond is relatively strong and unless a network of similar oxygen atoms exist within short distance of the proton, proton delocalization is unlikely. Furthermore, it was found that in ramsdellite, the protons prefer the pyramidal oxygen atom to the planar-coordinated oxygen atom. We believe that this difference is largely due to the electrostatic interactions between the proton and the Mn ions. When connected to the pyramidal oxygen, the proton is further away from Mn ions then when it is connected to the planar oxygen. This was confirmed by calculating the Madelung field at both sites. It is considerably more positive at the planar site. Calculations suggest that a proton in the octahedral sites is extremely unlikely in ramsdellite and groutite. However, in pyrolusite and manganite, there is a very large

relaxation of the structure on proton intercalation. This reduces the O-H...O distance and creates two shallow minima on each side of the octahedral site. Protons can easily hop between them (activation barrier ≈25 meV) and hence vibrate around the octahedral sites. This may explain the observations of Fillaux et al. and Fitzpatrick et al. Such hopping does not constitute diffusion, as it has no component along the tunnel-axis.

2. Proton diffusion

We have found a very wide range of activation barriers for proton diffusion in the common $MnOOH_x$ polymorphs. Ramsdellite has by far the lowest activation barrier for proton diffusion. Diffusion in this polymorph occurs by jumping across the tunnel through the rotation-and-jump mechanism. The large physical space in the 2×1 tunnels, often stated as the reason for high proton transport in ramsdellite, is not directly relevant to the fast proton migration. Rather, it is the topological connectivity of the pyramidal oxygen sites and their relation to the Mn ions that is important. Similar to what we observed when investigating the proton locations, we found that low-energy migration channels are in part determined by electrostatic interaction with Mn cations. Hydrogen atoms prefer not only to be covalently bonded to an oxygen but also to stay as far away as possible from the Mn cations. The activation barrier for proton migration in pyrolusite is considerably higher which may explain in part why its reduction is usually considered to be slow. Our results suggest that introduction of twinning defects as well as De Wolff disorder can have a large adverse effect on the proton diffusivity in MnO_2. Experimentally, it is found that the kinetics of reduction of γ-MnO_2 slows down towards the end of discharge [38], which has been attributed to reduced proton diffusivity. Our results confirm that this may be the case. Activation energies in the reduced polymorphs are considerably higher than in the unreduced polymorphs, for both ramsdellite and

pyrolusite. We believe this increase to be due to structural changes induced by Jahn-Teller distortions and interaction between the H atoms. Interestingly, our cluster expansion results suggest that direct H-H interactions are very weak for this system; instead, calculations in manganite indicate that the oxygen mediated indirect H-O-H interactions play a more significant role. Proton diffusion in manganite is along a path different from that of pyrolusite. Diffusion in pyrolusite occurs through a proton hop between neighboring oxygen atoms along the 1×1 tunnel. However, this diffusion path is unstable in manganite since the neighboring oxygen atom in manganite is already bonded to a proton on the other side of the tunnel and hence the proton has to traverse further to hop to a stable configuration, near an oxygen atom with no prior protons bonded to it. Thus, the H-O-H interaction is caused by one H taking up the oxygen bonding potential that another H needs to allow easy transport. This somewhat novel mechanism for protons impeding each other's transport needs further investigation to confirm its importance.

3. Voltage Curve

Intercalation calculations on the ramsdellite-groutite system indicate that H-vacancy interactions are weak and repel each other in the system. This leads to a phase separating system below T=200K. At room temperature, the entropy of mixing is strong enough to induce solid solution formation. Real γ-MnO_2 is probably better approximated as ramsdellite with some other phases that impose coherency strains on the ramsdellite units. Calculations suggest that this coherency strain can have a significant impact on the ordering behavior of the system. If the system is allowed to be incoherent during intercalation, groutellite is unlikely to be formed. The $MnOOH_x$ system will behave as a solid solution between ramsdellite (MnO_2) and groutite (MnOOH). However, if the

system is constrained to be coherent, the intermediate groutellite ($MnOOH_{0.5}$) phase is likely to be formed.

Comparison of a calculated discharge curve for perfect ramsdellite and experimental discharge curves indicates a discrepancy between the two curves at low reduction levels. Experimental differential voltage curves show a broad peak until x=0.2 (x corresponds to $MnOOH_x$), which is not observed in calculations on pure ramsdellite. However, intercalation calculations performed on ramsdellite with proton compensated Mn vacancies (i.e. Ruetschi defects) indicate that intercalated protons are more stable near these defects (and hence reduce at higher potential). We believe therefore that the discrepancy between calculated and experimental intercalation curves in figure 4.10 is due to the presence of Ruetschi defects in the experimental samples. These defects are probably the true source of the broad peaks in the differential voltage curve from x=0 to x=0.2. This peak has been attributed to surface protons but surface protons cannot explain the presence of a peak until x=0.2. Thus, Ruetschi defects play a significant role in the intercalation process of γ-MnO_2.

Chapter 5

Conclusion

In this research, we have performed a First Principles investigation of structure, defects and proton insertion in γ-MnO_2. This highly disordered material exhibits both technologically important and scientifically interesting properties. Currently, it is used as the cathode material for primary alkaline batteries.

We have focused on two aspects of γ-MnO_2.

(i) As a first step, we performed an extensive investigation of the structural stability of γ-MnO_2. Since γ-MnO_2 is characterized by configurational disorder, we implemented the cluster expansion formalism in combination with density functional first principles calculations to calculate the energy of any Mn-vacancy arrangement within the lattice at a given composition. This energy model was then used in conjunction with statistical mechanical methods to determine thermodynamic properties for the system.

Our structural calculations lead to the following conclusions:

- Pyrolusite is the ground state of stoichiometric MnO_2 when paramagnetic density functional theory (DFT) results are considered, which is in agreement with experiments. However, any structure that has perfect alternation of Mn atoms & vacancies along the c-axis has an energy very close to that of pyrolusite. Standard ferromagnetic spin polarization computations give incorrect results.
- Simulations suggest that thermal disorder is not the reason for the structural complexity in γ-MnO_2. If the system is governed by only thermodynamics,

stoichiometric MnO_2 should contain only pyrolusite at room temperature. Several thousand degrees are needed to induce disorder in stoichiometric pyrolusite MnO_2.

- Ruetschi defects could be the reason for the structural complexity of γ-MnO_2. Ruetschi defects stabilize ramsdellite and twinning over pyrolusite and introduce disorder in the material.

(ii) It is now commonly recognized that γ-MnO_2 electrodes in alkaline aqueous electrolytes behave mainly as intercalation electrodes. The discharge of the electrochemical cell occurs through proton and electron insertion into the MnO_2 host structure. We performed First Principles calculations to study proton location and dynamics in MnO_2. The results of these calculations are as follows:

- Protons are always covalently bonded to an oxygen atom in MnO_2. In ramsdellite, the proton prefers the pyramidal oxygen to the planar coordinated oxygen atom. In both pyrolusite and manganite, the protons may appear to be at an octahedral center in experiments as the activation barrier for hopping between the two stable sites on each side of the octahedral position is only about 25 meV.
- We found a very wide range of activation barriers in the common MnO_2/MnOOH polymorphs that we studied. Introduction of de Wolff disorder and twinning defects was found to have a large adverse effect on the proton diffusivity. Protonation also increases barriers to proton mobility, both due to structural changes induced by Jahn-Teller distortions and interaction between the H atoms. Calculations suggest that direct H-H interactions are not that significant compared to oxygen mediated indirect interactions, observed in manganite.
- H-vacancy interactions are fairly weak and repulse each other in the ramsdellite system (system phase separates into ramsdellite and groutite). The ordered phase,

observed in experiments at c=0.5 (groutellite), may be due to lattice remaining coherent during intercalation.

- Experimental and calculated ramsdellite discharge curves deviate significantly for $c \leq 0.2$. We believe that a significant source of this discrepancy is the presence of proton compensated Mn vacancies in real MnO_2, which create local sites with higher discharge potential.

Bibliography

[1] D. Linden, *Handbook of Batteries*, McGraw-Hill, New York (1994).

[2] J. Desilvestro and O. Hass, *J. Electrochem. Soc.* **137**, 5c (1990).

[3] A.F. Kohan, *Total-energy models for phase-stability studies in multicomponent oxides*, PhD thesis, Massachusetts Institute of Technology (1997).

[4] P. Hohenberg and W. Kohn, *Phys. Rev. B*, **136**, 864 (1964).

[5] W. Kohn and L. J. Sham, *Phys. Rev. A*, **140**, 1133 (1965).

[6] R. G. Parr, W. Yang, *Density-Functional Theory of Atoms and Molecules*, Oxford University Press, New York (1989).

[7] G. Ceder, M. K. Aydinol, A. F. Kohan, *Comp. Mat. Sci.*, **8**, 161 (1997).

[8] W. Zhong, D. Vanderbilt, K. M. Rabe, *Phys. Rev. B*, **52**, 6301 (1995).

[9] M. C. Payne, M. P. Teter, D. C. Allan, T. A. Arias, J. D. Joannopoulous, *Rev. Mod. Phys.*, **64**, 1045 (1992).

[10] K. M. Glassford and J. .R Chelikowsky, *Phys. Rev. B*, **46**, 1284 (1992).

[11] M. J. Gillian, I. Manassidis, A. De Vita, *Philos. Mag. B*, **69**, 879 (1994).

[12] Y. Bar-Yam, S. T. Pantelides, J. D. Joannopoulos, *Phys. Rev.B*, **39**, 3396 (1989).

[13] A. F. Kohan and G. Ceder, *Phys. Rev. B*, **54**, 805 (1996).

[14] M. K. Aydinol, A. F. Kohan, G. Ceder, K. Cho, J. Joannopoulos, *Phys. Rev. B*, **56**, 1354 (1997).

[15] G. Kresse and J. Furthmuller, *Phys. Rev. B*, **54**, 11169 (1996)

[16] G. Kresse and J. Furthmuller, *Comp. Mater. Sci.*, **6**, 15 (1994).

[17] G. Kresse and J. Hafner, *Phys. Rev. B*, **49**, 14251 (1994).

[18] D. Vanderbilt, *Phys. Rev. B*, **41**, 7892 (1990).

[19] D. M. Ceperley and B. J. Alder, *Phys. Rev. Lett.*, **45**, 566 (1980).

[20] J. P. Perdew and A. Zunger, *Phys. Rev. B*, **23**, 5048 (1981).

[21] H. J. Monkhorst and J. D. Pack, *Phys. Rev. B*, **13**, 5188 (1976).

[22] P. E. Blochl, O. Jepsen, O.K. Andersen, *Phys. Rev. B*, **49**, 16223 (1994).

[23] G. Ceder, *Comp. Mat. Sci.*, **1**, 144 (1993).

[24] S. K. Mishra and G. Ceder, *Phys. Rev. B*, **56**, 6120 (1999).

[25] A. van de Walle, PhD thesis, Massachusetts Institute of Technology (2000).

[26] J. M. Sanchez, F. Ducastelle and D. Gratias, *Physica*, **128A**, 334 (1984).

[27] K. Binder and D.W. Heermann, Monte Carlo Simulation in Statistical Physics, Springer-Verlag, Berlin (1988).

[28] S. K. Ma, Statistical Mechanics, World Scientific, Philadelphia (1985).

[29] D. Chandler, Introduction to Modern Statistical Mechanics, Oxford University Press, New York (1987).

[30] J. M. Yeomans, Statistical Mechanics of Phase Transitions, Clarendon Press, Oxford (1992).

[31] S. M. Foiles and J. B. Adams, *Phys. Rev. B*, **40**, 5909 (1989).

[32] N. Metropolis et al., *J. of Chem. Phys.*, **21**, 1087 (1953).

[33] G. Mills, H. Jonsson, G. K. Schenter, *Surf. Sci.*, **324**, 305 (1995).

[34] P. Saul, C. R. A. Catlow, J. Kendrick, *Philos. Mag. B.*, **51**, 107 (1985).

[35] J. P. Gabano, J. Seguret and J. F. Laurent, *J. Electrochem. Soc.*, **117**, 147 (1970).

[36] M. P. Allen and D. J. Tildesley, *Computer Simulation of Liquids*, p. 71, Clarendon Press, Oxford (1987).

[37] O. Schilling and J. R. Dahn, *J. Appl. Cryst.*, **31**, 396 (1998).

[38] Y. Chabre and J. Pannetier, *Progress in Solid State Chemistry*, **23**, 1 (1995).

[39] A. H. Heuer, A. He, P. Hughes and F. Feddrix, IBA 2000 Manganese Oxide Symposium (Argonne, III. May 9-12, 2000).

[40] P. M. De Wolff, J. W. Visser, R. Giovanoli and R. Brutsch, *Chimia*, **32**, 257 (1978).

[41] P. M. De Wolff, *Acta Cryst.*, **12**, 341 (1959).

[42] D. E. Simon, T. N. Anderson and C. D. Elliott, IBA 2000 Manganese Oxide Symposium (Argonne, III. May 9-12, 2000).

[43] J. C. Charenton and P. Strobel, *J. Solid State Chem.*, **77**, 33 (1988).

[44] W. Bowden, R. Sirotina and S. Hackney, IBA 2000 Manganese Oxide Symposium (Argonne, III. May 9-12, 2000).

[45] A. Guinier, X-Ray Diffraction, W. H. Freeman and Co., San Francisco (1963).

[46] M. Kaburagi and J. Kanamori, *J. Phys. Soc. Japan*, **44**, 718 (1978).

[47] W. Bowden, F. Wang, Y. Palk and C. Grey, IBA 2000 Manganese Oxide Symposium (Argonne, III. May 9-12, 2000).

[48] D. de Fontaine, G. Ceder and M. Asta, *J less-common met*, **164**, 108 (1990).

[49] A. Kozawa, *J. Electrochem. Soc.*, **106**, 79 (1959).

[50] A. J. Brown, F. L. Tye and L. L. Wood, *J. Electroanal. Chem.*, **122**, 337 (1981).

[51] E. Preisler, *J. Appl. Electrochem*, **6**, 311 (1976).

[52] P. Broulliet, A. Grund and F. Jolas, *C. R. Acad. Sci. Paris*, **257**, 3166 (1963).

[53] G. Coeffier and J. Brenet, *Electrochim. Acta*, **10**, 1013 (1965).

[54] P. Ruetschi, *J. Electrochem. Soc.*, **131**, 2737 (1984).

[55] P. Ruetschi, *J. Electrochem. Soc.*, **135**, 2657 (1988).

[56] R. Giovanoli, *Thermochim. Acta*, **234**, 303 (1994).

[57] J. Fitzpatrick, L. A. H. Maclean, D. A. J. Swinkels, F. L. Tye, *J. Applied Electrochem.*, **27**, 243 (1997).

[58] F. Fillaux, C. H. Cachet, H. Ouboumour, J. Tomkinson, C. Levy-Clement and L. T. Yu, *J. Electrochem. Soc.*, **140**, 585 (1993).

[59] L. S. D. Glasser and L. Ingram, *Acta Cryst.*, **B24**, 1233 (1968).

[60] H. Dachs, *Z. Krist.*, **118**, 303 (1963).

[61] T. Kohler, T. Armbruster, E. Libowitzky, *J Solid State Chem.*, **133**. 486 (1997).

[62] P. Brouillet, A. Grund, F. Jolas and R. Mellet, *C. R. Acad. Sc. Paris*, **257**, 3390 (1963).

[63] G. S. Bell and R. Huber, *J. Electrochem. Soc.*, **111**, 1 (1964).

[64] W. C. Maskell, J. E. A. Shaw and F. L. Tye, *Electrochim. Acta*, **26**, 1403 (1981).

[65] A. Kozawa and J. F. Yeager, *J. Electrochem. Soc.*, **112**, 959 (1965).

[66] J. W. D. Connolly and A. R. Williams, *Phys. Rev. B*, **27**, 5169 (1983).

THESIS PROCESSING SLIP

FIXED FIELD: ill. _____ name _____

index _____ biblio _____

▶ COPIES: (Archives) Aero Dewey Barker Hum

Lindgren Music Rotch (Science) Sche-Plough

TITLE VARIES: ▶ ☐ _____

_____

_____

NAME VARIES: ▶ ☐ _____

_____

IMPRINT: **(COPYRIGHT)** _____

_____

▶ COLLATION: _____

_____

▶ ADD: DEGREE: _____ **▶ DEPT.:** _____

▶ ADD: DEGREE: _____ **▶ DEPT.:** _____

SUPERVISORS: _____

_____

NOTES:

cat'r: date:

page:

▶ DEPT: [illegible]

▶ YEAR: [illegible] **▶ DEGREE:** [illegible]

▶ NAME: [illegible]

_____